PRODUCTION AND CHARACTERIZATION OF EMULSION DERIVED POROUS SiOC+TiO_2 SUBMICRON/NANOSPHERES

A Thesis Submitted to
the Graduate School of
İzmir Institute of Technology
in Partial Fulfillment of the Requirements for the Degree of

MASTER OF SCIENCE

in Materials Science and Engineering

by
Öykü İÇİN

July 2020
İZMİR

ACKNOWLEDGMENTS

Firstly, I would like to thanks to my advisor, Assoc. Prof. Dr. Çekdar Vakıf AHMETOĞLU, for his guidance throughout this journey.

I want to thank the members of our research group ‘’Inorganic Solid Materials Group’’ at IZTECH including Tuğçe SEMERCİ, Ezgi OĞUR, Ecem ÖZMEN, Beyza HASDEMİR, Levent KARACASULU, Cerem PİŞKİN, and Esin KARATAŞ for their friendship and support.

I would like to thank Assoc. Prof. Dr. Ümit Hakan YILDIZ and his MSc. student Soner KARABACAK for their help and for letting me use the sonicator in the laboratory.

I would like to thank the members of the Metal Studio at IZTECH for helping the design and construction of the UV cabinet system.

I would like to thank the team of MAM (Center for Materials Research) at IZTECH for helping me complete analyses that are missing in this pandemic days.

A special thanks to my fiance, Aytuğ ERDEMİR for always being with me during this bittersweet journey.

I wish to thank all of my family and friends for their supports.

ABSTRACT

PRODUCTION AND CHARACTERIZATION OF EMULSION DERIVED POROUS SiOC+TiO_2 SUBMICRON/NANOSPHERES

The water resources are polluted because of the widespread use of dyes in the industry, resulting in a major ecological threat. Among the various water treatment techniques, adsorption and photocatalytic degradation methods are the most preferred owing to their easy applicability, low cost, and high efficiency. Silicon oxycarbide (SiOC), which is a type of polymer-derived ceramic, has the potential to be used in harsh environmental conditions thanks to its strong chemical stability and oxidation resistance, that being said it can also be used as a photocatalyst substrate. Titanium dioxide (TiO_2) photocatalysts are extensively used for purification of contaminated waters. And also, TiO_2 particles are synthesized with various material groups to investigate the adsorption and photocatalytic effect. In this thesis, initially, submicron/nano SiOC spheres were produced via an oil in water (o/w) emulsion technique by using parameters such as two types of preceramic polymer precursors (silicon oil and resin), mixing types (magnetically and ultrasonically), and different pyrolysis temperature (600-1200 ^oC). Upon the formation of submicron/nano SiOC spheres, selected samples were impregnated with a different molar of titanium oxide precursor solution (Titanium(IV) n-butoxide (TBT)) and calcined at 450 °C for 4 h. Various amounts of (0-5-10-20 wt.%) TiO_2 containing submicron/nano SiOC spheres were produced and then characterized in depth by various techniques. Finally, the effects of pyrolysis temperatures and the amount of TiO_2 were investigated in terms of adsorption and photocatalytic performance against aqueous cationic dye (methylene blue) (MB) solution. In the adsorption experiments, pure SiOC submicron/nanospheres (UM1200), pyrolyzed at 1200 ^oC, showed the best performance at the end of 24 h in the dark with 64% adsorption. In photocatalytic experiments, samples obtained by coating the SiOC substrate produced by pyrolysis at 600 ^oC with different amounts of TiO_2 (UM600T5, UM600T10 and UM600T20) showed 79%, 80%, and 87% photodegradation efficiency.

ÖZET

EMÜLSİYON İLE GÖZENEKLİ SiOC+TiO_2 MİKRONALTI/NANOKÜRECİKLERİN ÜRETİMİ VE KARAKTERİZASYONU

Boyaların endüstride yaygın olarak kullanılması su kaynaklarında kirliliğe neden olmaktadır ve bu da büyük bir ekolojik tehdit oluşturmaktadır. Çeşitli su arıtma teknikleri arasında, adsorpsiyon ve fotokatalitik bozunma yöntemleri kolay uygulanabilirliği, düşük maliyeti ve yüksek verimliliği sayesinde en çok tercih edilenlerdir. Polimer türevli bir seramik türü olan silikon oksikarbür (SiOC), güçlü kimyasal stabilitesi ve oksidasyon direnci sayesinde sert çevre koşullarında kullanılma potansiyeline sahiptir ve bu sayede bir fotokatalist substratı olarak da kullanılabileceği söylenilebilir. Titanyum dioksit (TiO_2) fotokatalistleri, kirli suların temizlenmesi için yaygın olarak kullanılmaktadır. Ayrıca TiO_2 partikülleri, adsorpsiyon ve fotokatalitik etkiyi araştırmak için çeşitli malzeme grupları ile sentezlenmektedir. Bu tezde, ilk olarak, micron-altı/nano SiOC küreler, iki tip öncü preseramik polimeri (silikon yağı ve reçine), karıştırma tipleri (manyetik ve ultrasonik) ve farklı piroliz sıcaklıkları (600-1200 ^oC) gibi parametreler kullanılarak su içinde yağ (o / w) emülsiyon tekniği ile üretilmiştir. Mikron-altı/nano SiOC kürelerinin elde edilmesi üzerine seçilmiş numuneler farklı molaritelerde titanyum oksit öncü çözeltisi (Titanyum (IV) n-butoksit (TBT)) ile emdirme işlemine ve 450 ° C'de 4 saat kalsinasyona tabi tutulmuştur. Çeşitli miktarlarda (ağırlıkça% 0-5-10-20) TiO_2 içeren micron-altı/nano SiOC küreleri üretilmiş ve çeşitli tekniklerle derinlemesine karakterize edilmiştir. Son olarak, piroliz sıcaklıklarının ve TiO_2 miktarının etkisi sulu katyonik boya (metilen mavisi) (MB) çözeltisine karşı adsorpsiyon ve fotokatalitik performans açısından araştırılmıştır. Adsorpsiyon deneylerinde, 1200 ^oC'de pirolize edilerek üretilen saf SiOC micron-altı/nanoküreleri (UM1200), 24 saat sonunda %64 adsorpsiyon ile en iyi performansı göstermiştir. Fotokatalitik deneylerde ise, 600 °C' de pirolize edilerek üretilen SiOC substratının farklı miktarlarda TiO_2 ile kaplanması ile elde edilen numuneler (UM600T5, UM600T10 ve UM600T20) % 79, % 80 ve % 87 fotodegradasyon verimi göstermişlerdir.

Dedicated to my grandmother…

TABLE OF CONTENTS

LIST OF FIGURES

Figure **Page**

Figure **Page**

Figure **Page**

Figure **Page**

Figure **Page**

Figure **Page**

Figure **Page**

LIST OF TABLES

Table **Page**

CHAPTER 1

INTRODUCTION

1.1. Motivation

Water is one of the basic needs for all humans to survive and covers approximately 70% of the Earth's surface.[1, 2] The fact that the majority of all water (97%) is in the oceans makes only %1 of water in the world possible to be usable by humans.[2] It is also known that quality and safe water are necessary for human development and well-being.

Even though the benefits of industrialization are numerous, the development of industrialization has led to an increase in water pollution.[3, 4] Water pollution can be described as changing the quality of the water by physical, chemical, biological and radiological pollutants.[3, 5] Major causes of water pollution are domestic sewage, population growth, and industrialization.[5]. The discharge of wastewater from various plants such as factories and laboratories to the environment is a serious problem.

According to the World Health Organization (WHO), drinking water resources are directly damaged due to the improper treatment of industrial and agricultural wastewater, which brings about a million people's death every year.[6]

Increasing environmental pollution problems attract the attention of researchers. In this context, researchers are trying to solve this problem by producing suitable and effective materials thanks to developing technologies. So, studies in this field are increasing every year. It can be seen clearly from data of the *web of science* search with the various keywords "wastewater treatment", "wastewater recovery", "wastewater cleaning", "polluted water cleaning", "polluted water recovery", "polluted water treatment" and "water pollution" related to materials science and multidisciplinary sciences are shown in Figure 1.1.

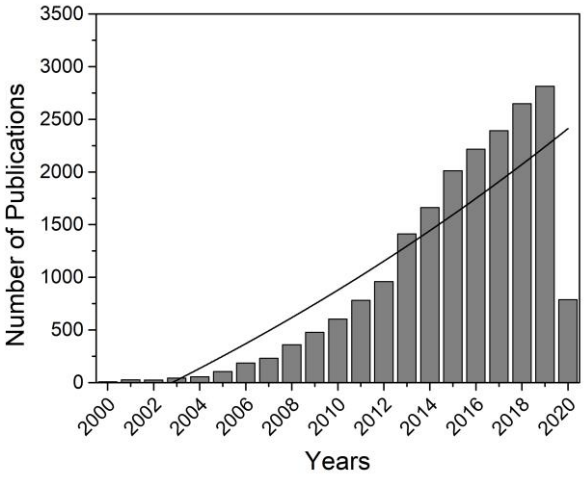

Figure 1. 1. The number of publications resulting from a web of science search with the keywords “wastewater treatment”, “wastewater recovery”, “wastewater cleaning”, “polluted water cleaning”, “polluted water recovery”, “polluted water treatment” and “water pollution”. Data was extracted from 2000 up to now and the line represents an exponential growth function fit.

(Source: Web of Science, 2020, May)

1.2. The Structure and Content of the Thesis

The first chapter elaborately addresses the objective of the thesis, waste-water problems, treatment methods, structure and properties of materials, the literature review related to silicon oxycarbide (SiOC) micron and submicron spheres, emulsion derived SiOC structures and adsorption & photocatalytic performance on cationic methylene blue (MB) dye of these materials.

The detailed experimental procedure of the SiOC+TiO_2 submicron/nanospheres production is illustrated in Chapter 2.

The characterization of samples, their adsorption & photocatalytic performance on methylene blue dye, and the discussions are addressed in Chapter 3.

Finally, the conclusions of the study are given in Chapter 4.

1.3. Dyes

The widespread use of dyes in the industry (in textile, cosmetics, medicine, food, paper, and paint industries) causes pollution in water, and dyes mixed into water resources are considered to be a serious threat to ecosystem.[7-10] Approximately 1-20% of the world's total dye supply is released by textile wastewater as a result of various processes.[11]

When dyes (either toxic or carcinogenic) mix into the water, they reduce light penetration and photosynthesis.[12] And also, they become more stable and not biodegraded because of their complex aromatic molecular structures.[13, 14] Therefore, removing dyes from industrial wastewater is a critical issue for the environment.[14]

Dyes can be categorized as anionic (acid, direct, and reactive), cationic (basic) and nonionic dyes (disperse and vat) according to their ionic structure.[15, 16]

1.3.1. Anionic Dyes

Anionic dyes are water-soluble compounds, comprising acid, direct and reactive dyes. Due to negative ions in the structure, these dyes can be attached to a cationic (positively charged) substance (wool, silk, and acrylic fibers).[16] Chemical structures of some anionic dyes are shown in Figure 1.2.

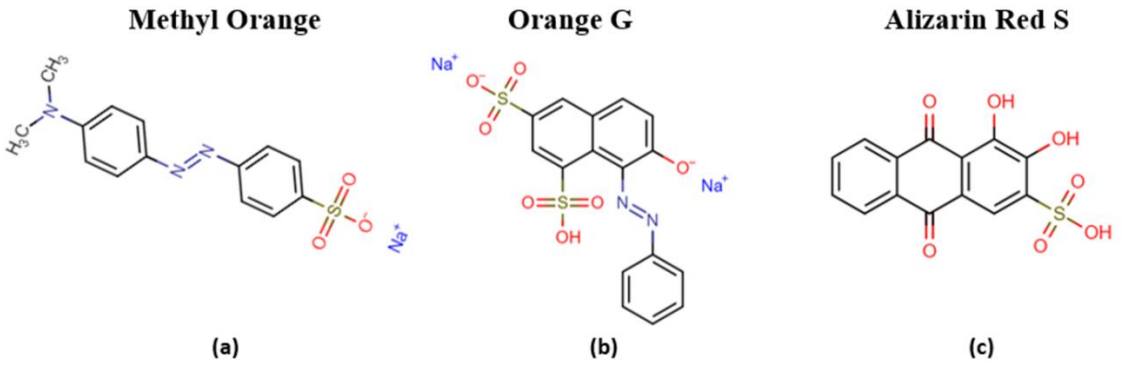

Figure 1. 2. The chemical structure of (a) Methyl Orange, (b) Orange G, and (c) Alizarin Red S anionic dye molecules.
(Sources: Chemicalize, 2020, May; Zhang, W et al., 2018)[17, 18]

1.3.2. Non-ionic Dyes

Non-ionic dyes, insoluble in water, have two types which are disperse and vat dyes.[16] Chemical structures of some non-ionic dyes are shown in Figure 1.3.

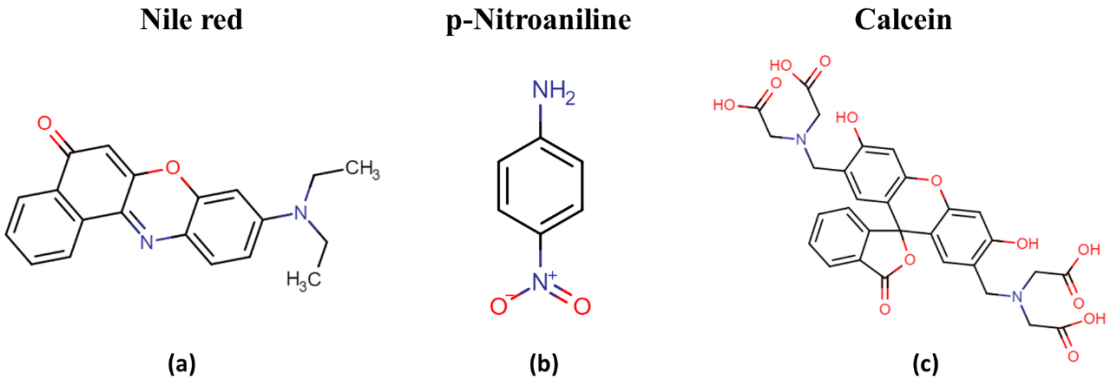

Figure 1. 3. The chemical structure of (a) Nile red, (b) p-Nitroaniline, and (c) Calcein nonionic dye molecules.
(Sources: Chemicalize, 2020, May; Zhang, W et al., 2018)[17, 18]

1.3.3. Cationic Dyes

Among other dye classes, cationic dyes give colored cations to the solution when dissolved in water. Therefore, they are called cationic dyes. Cationic dyes are commonly used for paper, silk, cotton, wool, nylons & polyesters, cation dyeable polyethylene dyeing, and also medicine industry owing to their ease of application, durability, and high fastness to materials.[15] However, their adverse effects on the ecosystem are considerable due to their carcinogenic & mutagenic and strong coloring impacts when discharged into the water.[19, 20] Some cationic (basic) dye molecules are shown in Figure 1.4.

Methylene blue (MB) is a type of cationic dye with the $C_{16}H_{18}N_3SCl$ molecular formula, shown in Figure 1.4 (c).[21] It is frequently used in textile, paper, printing, and other industries. So, it can be found in the wastewater of these industries. Even a small amount of dye in wastewater (<1 ppm)[22-25] harms the environment directly or indirectly.

For example; in case of direct contact or inhalation, it can cause eye burns, vomiting, nausea, sweating, mental confusion.[22, 24, 26, 27]

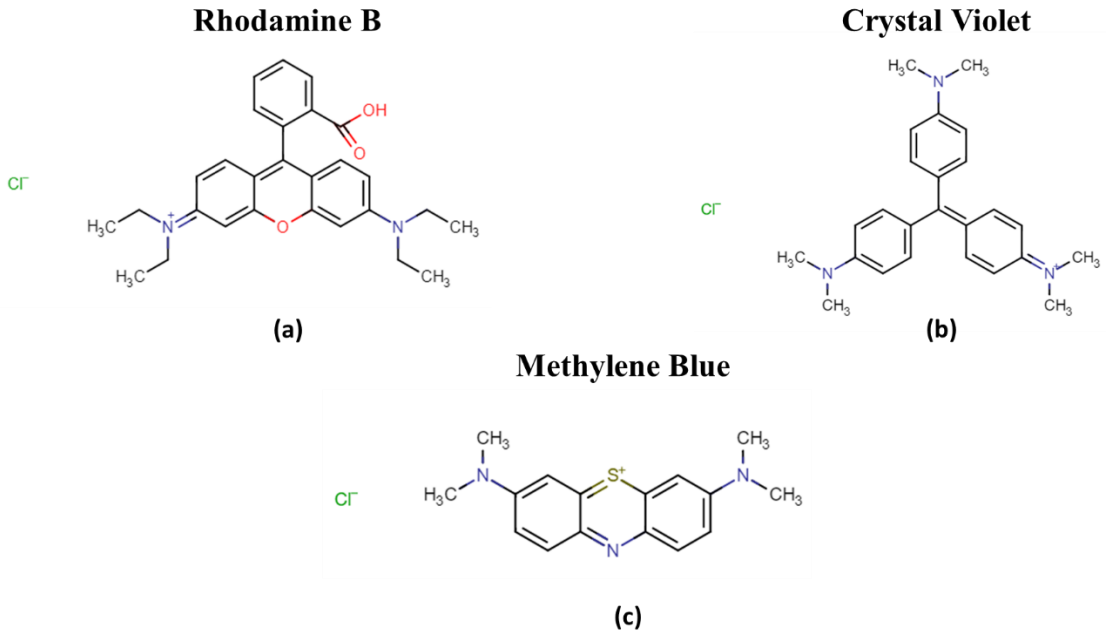

Figure 1. 4. The chemical structure of (a) Rhodamine B, (b) Crystal Violet, and (c) Methylene Blue cationic dye molecules.

(Sources: Chemicalize, 2020, May; Zhang, W et al., 2018; Zeydanli, D. et al., 2018)[17, 18, 28]

According to literature, in the studies where silicon oxycarbide (SiOC) was used as an adsorbent material, cationic dyes were selected for adsorption experiments.[10, 25, 28-30] It is considered that bonds and interactions occur between materials having functional (radical) groups on the surface and cationic dye molecules.[31]

In this thesis, SiOC will be used as an adsorbent material. Due to the functional surface properties of SiOC, methylene blue (MB) cationic dye will be used in measuring the adsorption performance.

1.4. Polluted Water Treatment Methods

Rapid and easy removing of dyes from wastewater is a serious environmental issue that needs careful consideration.[14, 32] Various physical, chemical, and biological systems have been developed to remove dyes from water: they are generally divided into two categories based on separation (physical adsorption, coagulation, ion exchange, and membrane process) and degradation (biodegradation, chemical oxidation-reduction, electrochemical oxidation, photocatalytic degradation).[7, 15, 22, 33] Among them, adsorption and photocatalytic degradation are considered as the simplest, green, inexpensive and effective technology among traditional wastewater treatment technologies.[9, 10, 34, 35]

1.4.1. Adsorption

Among conventional wastewater treatment technologies, the adsorption phenomenon has been known since the 17th century.[36, 37] It is an effective method commonly used for the decontamination of organic pollutants (especially dyes) from the aqueous media.[37] It is considered superior to other techniques thanks to its low cost (approx. 10 to 200 US$ per million liters)[38], removal efficiency (90–99%)[38], ease of application, and non-toxicity as a final product.[7, 24, 35, 37, 39]

Adsorption is explained by the surface phenomenon between adsorbent and adsorbate (pollutant compounds).[38] The principle of adsorption technique, used to eliminate contaminants from wastewater, is the adhering of the pollutants (in a liquid or gas phase) on a solid adsorbent. Adsorbate can be also defined as a substance that concentrates on the surface of adsorbent solids.[40] At the adsorption process, solid adsorbent substances are shaken with the wastewater. The contaminants bind to the surface and the equilibrium stage, in which both the adsorbed and the pollutant concentrations in the water are constant, is created.[38]

The types of adsorption mechanisms are chemical (chemisorption) and physical (physisorption) adsorption.[15] In physical adsorption, weak forces (Van der Waals, hydrogen bonding, and electrostatic forces) are active between atoms or molecules, whereas chemical adsorption involves a strong interaction (chemical bonds).[41] Whereas physical adsorption is reversible, chemical adsorption is irreversible. Besides, a multimolecular layer is formed in physical adsorption, while a unimolecular layer is

formed in chemical adsorption. [41] Figure 1.5 shows the basic mechanism of physical and chemical adsorption.

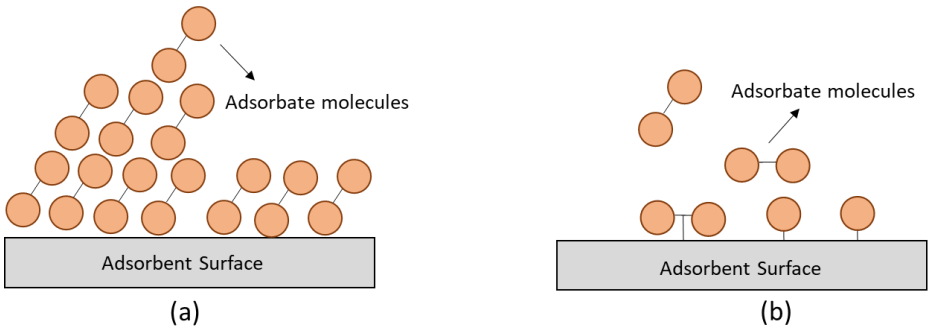

Figure 1. 5. The schematic presentation of; (a) physical and (b) chemical adsorption mechanism.

Some parameters have effect upon the adsorption process; these are solution conditions (Temperature, Ph, the concentration of pollutants and contact time), structure, composition, and particle size of the adsorbate and adsorbent.[38, 39]

Many researchers have examined the adsorption of dye at the solid/liquid interface and developed various adsorbents for purification of MB dye contaminated water.[4, 19] Some of these materials are alumina[42], silica gel[43], zeolites[44, 45], activated carbon[46], graphene oxide[47], and polymer derived ceramics (SiOC)[28].

1.4.2. Photocatalytic Degradation

Physical techniques like adsorption are used to remove dyes from water; however, these methods are restricted only to the transportation of chemical contaminants from water to different mediums, causing secondary contamination.

Such methods of physical separation increase the cost, and the adsorbent needs to be constantly renewed. Therefore, the use of photocatalysis in removing dyes from wastewater is more attractive because it can fully mineralize target pollutants and does not cause secondary pollution.[6, 11, 48]

Photocatalysts are semiconductors activated by absorbing photons of sufficient energy corresponding to the bandgap and are not consumed at the end of the reaction.[49] Photocatalytic oxidation technology is a commonly used method in wastewater treatment due to its high efficiency and not generating secondary pollution.[50] A good photocatalyst should be both biologically and chemically inert, as well as photo-stable, low cost, and non-toxic.[48] Examples of semiconductor photocatalysts are TiO_2, ZnO, Fe_2O_3, CdS, ZnS, SnO_2, WO_3 and WSe_2.[48, 49] Among the various semiconductors, Titanium dioxide (TiO_2) is one of the high potential photocatalysts owing to its wide bandgap (3.2 eV), hydrophilic, strong oxidizing ability, physical and chemical stability, low toxicity and cost.[48-51]

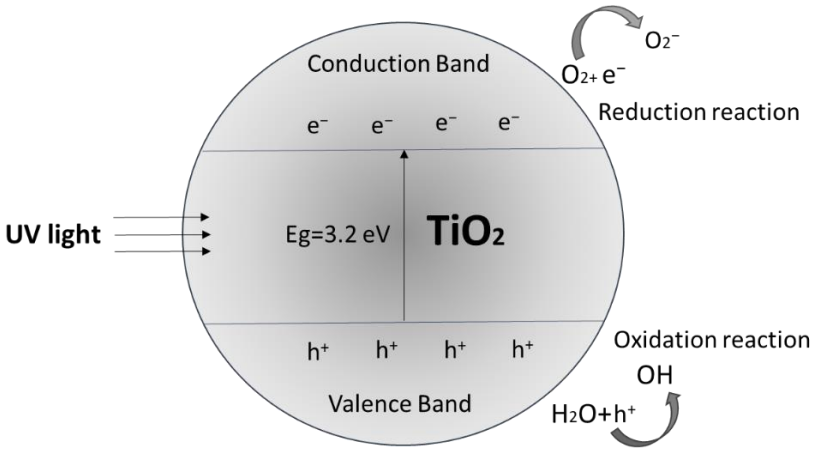

Figure 1. 6. The schematic presentation of TiO_2 photocatalytic mechanism.

The basis of the photocatalytic degradation process of TiO_2 is shown in Figure 1.6 and can be explained as follows: when a semiconductor photocatalyst is exposed to a suitable light source with higher than its bandgap energy, it causes the formation of electron/hole pairs (e_{CB}^-; reducing agent and h_{VB}^+; oxidizing agent). These electron/hole pairs trigger a series of chemical reactions that mineralize contaminants. These reactions are divided into two categories; oxidation and reduction reactions. In the valance band, holes (h_{VB}^+) diffuse to surface of photocatalyst and reacts with water, thus hydroxyl radicals (•OH) are generated and this process is termed as an oxidation reaction. The electrons (e_{CB}^-) in the conduction band react with oxygen (O_2) and form anion radical

superoxide. As a result of further reactions, hydroxyl radicals (•OH) are formed and this is known as the reduction reaction. And finally, hydroxyl radicals react with organic pollutants to produce water (H_2O) and carbon dioxide (CO_2) as end products.[49, 51]

Within the scope of the thesis, the photocatalytic performance of the SiOC+TiO_2 samples on cationic MB dye is addressed with a detailed literature review.

1.5. Emulsion Systems

The emulsion can be defined as heterogeneous systems in which two different liquids are immiscible with each other, but appear homogeneous.[52] Emulsions consist of two phases that are the hydrophilic phase and the lipophilic phase. These two phases are called the internal phase (dispersed phase) and the external phase (continuous phase) of the emulsion according to their role in the system.[53] These two immiscible separate phases can be combined stably with the aid of surfactants (surface active agents) that have hydrophilic and lipophilic parts. Surfactants typically act by reducing the surface tension and by weakening the forces that separate the oil and water phase. When the surfactant concentration increases, micelles begin to form. For the formation of micelles (as is shown in Figure 1.7), it is important to use the minimum concentration of surfactants that is known as the "critical micelle concentration".[54]

Considering the dispersed phase and droplet size, the emulsions are divided into several types. Based on the dispersed phase, emulsion types are; oil in water (o/w) and water in oil (w/o), also multiple systems; oil in water in oil (o/w/o) and water in oil in water (w/o/w), shown in Figure 1.8.

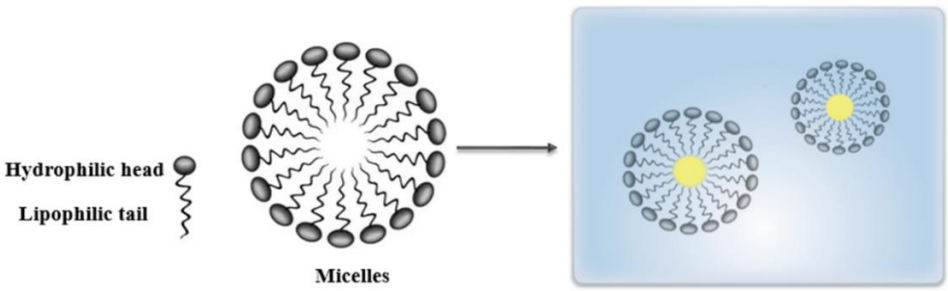

Figure 1. 7. The schematic drawing of micelles formation.

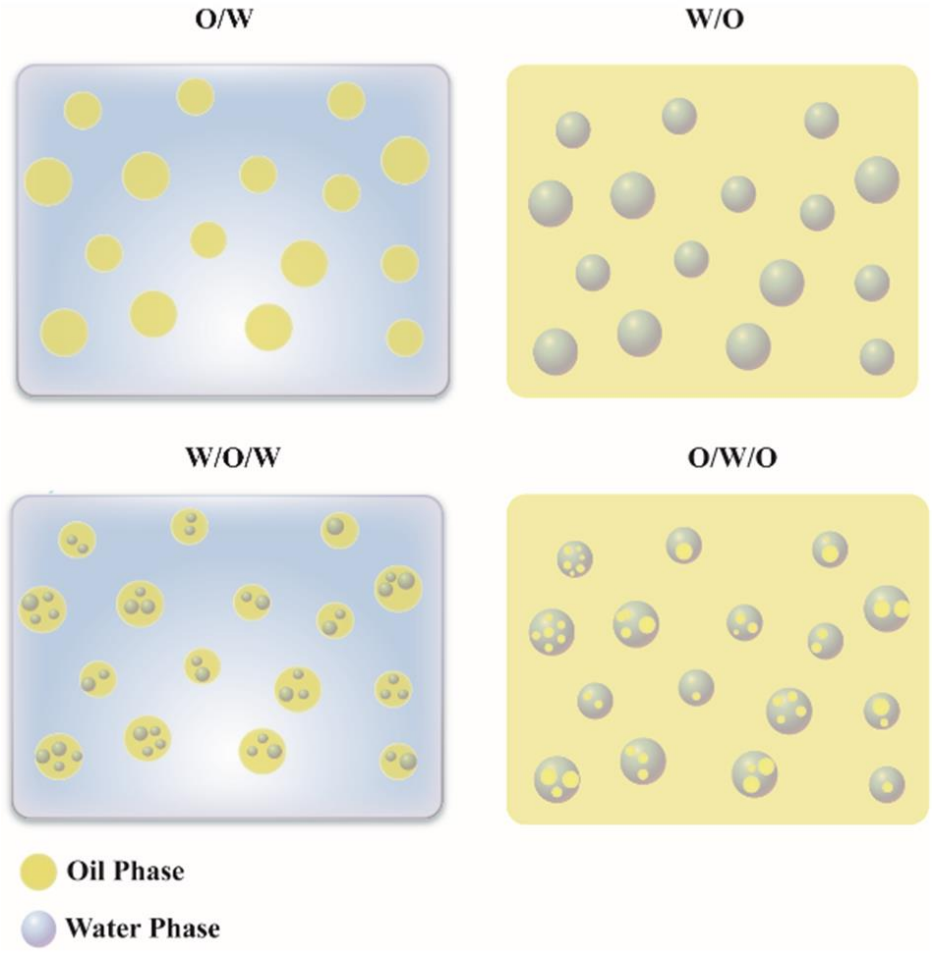

Figure 1. 8. The structure of emulsion types.

Based on the droplet size, emulsions are categorized as macro and mini emulsion. According to IUPAC (International Union of Pure and Applied Chemistry), the mini emulsion (submicron emulsion) is defined as the emulsion system having a dispersed phase with a droplet diameter of about 50 nm to 1 µm.[55, 56] On the other hand, the macro emulsion system has droplets size in the range of 1 to 100 µm.[56]

For the emulsion formation, it is necessary to energize the mixture through processes such as mixing, shaking, and homogenization. Some techniques are used to form mini emulsion systems. These are high energy methods (high-pressure homogenizer, ultrasonication, and micro-fluidization) and low energy methods.[57, 58] Ultrasonication has been used to make miniemulsion for over 50 years for the purpose of synthesizing nanomaterials.[59]

1.6. Polymer Derived Ceramics

Polymer-derived ceramics (PDCs) are produced through the processing and controlled heat treatment of preceramic polymers, usually containing Si atom in their backbone. Typical groups of organosilicon preceramic polymers are shown in Figure 1.9. These precursor polymers such as polycarbosilanes, polysiloxanes, polysilazanes, and polyborosilanes are used to obtain multicomponent ceramic materials; silicon-carbide (SiC), silicon-oxycarbide (SiOC)[60], silicon-carbonitride (SiCN)[60] and silicon-boroncarbonitride (SiBCN).

Polymer to ceramic transformation steps are shown in Figure 1.10 and consist of the following process; i) shaping of preceramic polymer, ii) crosslinking, and iii) converting to the ceramic component via heat treatment (at inert atmosphere and suitable temperatures).

Initially, preceramic polymers are transformed into thermoset structures via a curing process. With an effective crosslinking, precursor polymers have strongly interconnected backbone structures, so that the volatility of the crosslinked product can be reduced and therefore ceramic yield can be increased.[61] After crosslinking, the pyrolysis process is conducted in the range of 600- 1400 °C under inert conditions. During pyrolysis, the bonds of some molecules in the polymer main structure are broken. Throughout ceramization (organic-inorganic transition) redistribution reactions occur between Si – O, Si – C and Si – H bonds.[62] Besides, weight loss (10-30 wt.%.)[63] is observed around 800-1000 ^{o}C because of the release of various organic volatile gases (CH_4, C_6H_6, H_2, etc.). In consequence of decomposition of the organic moieties, transient micro-porosity occurs at low pyrolysis temperature (500-800 ^{o}C), and these transient pores disappear with the rising pyrolysis temperature.[64]

On the other hand, "free carbon" precipitation begins in certain areas. Due to the presence of free carbon, the color of material gradually turns black, “Ceramer” (ceramer = ceramic + polymer is the derived name for this material), which is brown above 600 ° C, turns black above 800 ° C, and therefore this amorphous material is also called “black glass”. These materials produced from preceramic polymers are defined as an amorphous material up to 1200 ° C.[65] When the pyrolysis temperature is increased, the units called the Basic Structural Unit (BSU) begin to grow; as a result, crystals are first seen in the nano-order, then grow larger and reach micron size.[66, 67]

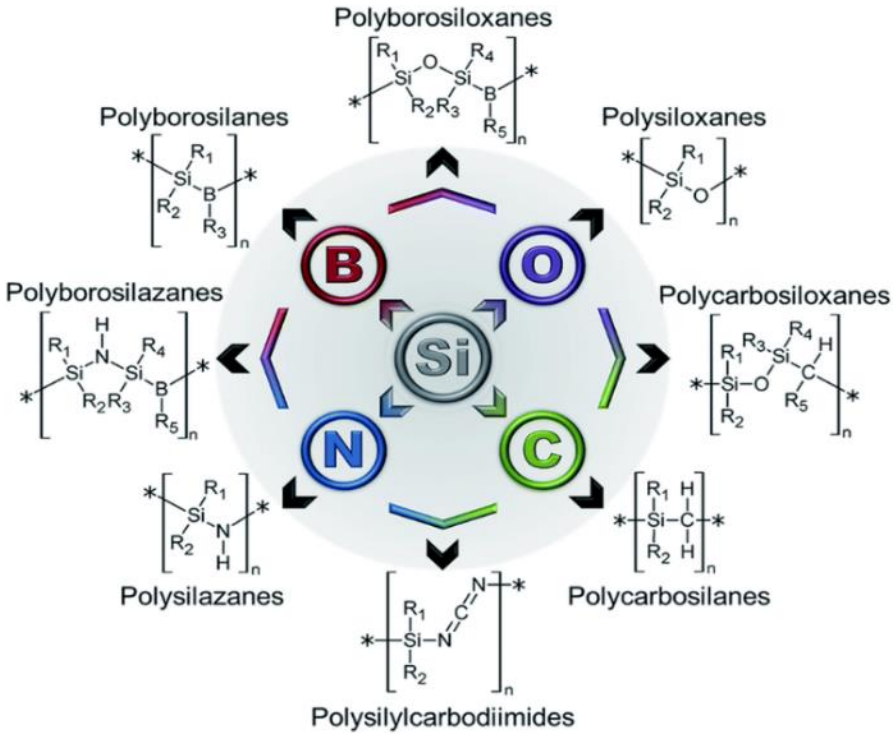

Figure 1. 9. The classification of silicon-containing preceramic polymers.

(Source: Barroso, G. et al., 2019)[68]

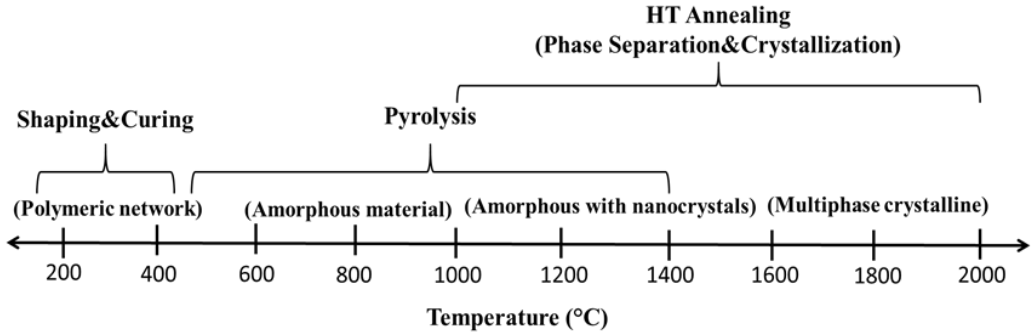

Figure 1. 10. The scheme of polymer to ceramic transformation.

Polymer-derived ceramic processing has many advantages over traditional ceramic production methods i.e; commercial availability of low-cost preceramic polymers, the ease of preceramic polymers' shaping via low cost & conventional

polymer-forming techniques, production of ternary complex molecular structure ceramics based on preceramic polymer chemistry, lower processing temperatures for production of advanced ceramics than conventional sintering of ceramic powders.[60, 66, 69, 70]

1.6.1. Silicon Oxycarbide (SiOC)

Silicon oxycarbide (black glass) is a type of glass that is a compound of silicon, oxygen, and carbon. Silicon oxycarbide ceramics have a general formula of SiO_xC_{4-x} ($0<x<4$) and excess carbon (C_{free}). Silicon atoms are tetrahedrally bound by oxygen and carbon atoms.[70, 71] If the "x" value in SiO_xC_{4-x} ($0 <x <4$) is changed, the sizes/amounts of silica and other units vary. Depending on initial polymer composition, pyrolysis temperature, and duration, within the SiOC ceramics, SiC_4, SiC_3O, SiC_2O_2, and SiO_4 units can be found in different ratios.[72] During polymer-ceramic transformation, with increasing pyrolysis temperature, structural changes are shown in Figure 1.11.

As shown in Figure 1.11, at lower (800-1000 ° C) pyrolysis temperatures, SiOC has a structure that comprises a homogeneous tetrahedra network of Si – C – O and excess carbon. With increasing pyrolysis temperature (1100-1300 ° C), amorphous silica (SiO_2) nanodomains are formed and they are embedded in SiOC mixed bonds (1–2 nm thick interlayer). And also, the cage-like network of sp2 graphene carbon surrounds these units in the form of an interconnected network. At higher temperatures (> 1400 ° C), phase-separation occurs in the amorphous SiOC network. These are silica-rich phase and a carbon-rich phase, interpenetrating nano-sized networks. Also, β-SiC nanocrystals (2–3 nm) precipitate at the interface between the SiO_2 domains and the walls of graphene cells. The initiation of β-SiC crystallization in SiOC glasses depends on the carbon content. For low carbon content SiOC glasses, the pyrolysis temperature required for the precipitation of the SiC crystal is lower (1200 ° C) than that of high carbon SiOCs (1400 ° C).[73]

Among preceramic polymers, polysiloxanes are used to prepare complex ternary SiOC ceramics with different forms (micro/nanospheres, fibers, foams, coatings, porous parts, etc.) [66, 76] Silicon oxycarbide ceramics have superior oxidation & creep resistance, chemical, high-temperature, mechanical stability, and biocompatibility.[77-80] Thanks to their excellent properties, SiOCs can be used for application areas such as high-temperature reaction catalysts, high-temperature-resistant structural materials, anodes of lithium batteries[81], adsorbent[28], medical applications.[71, 82]

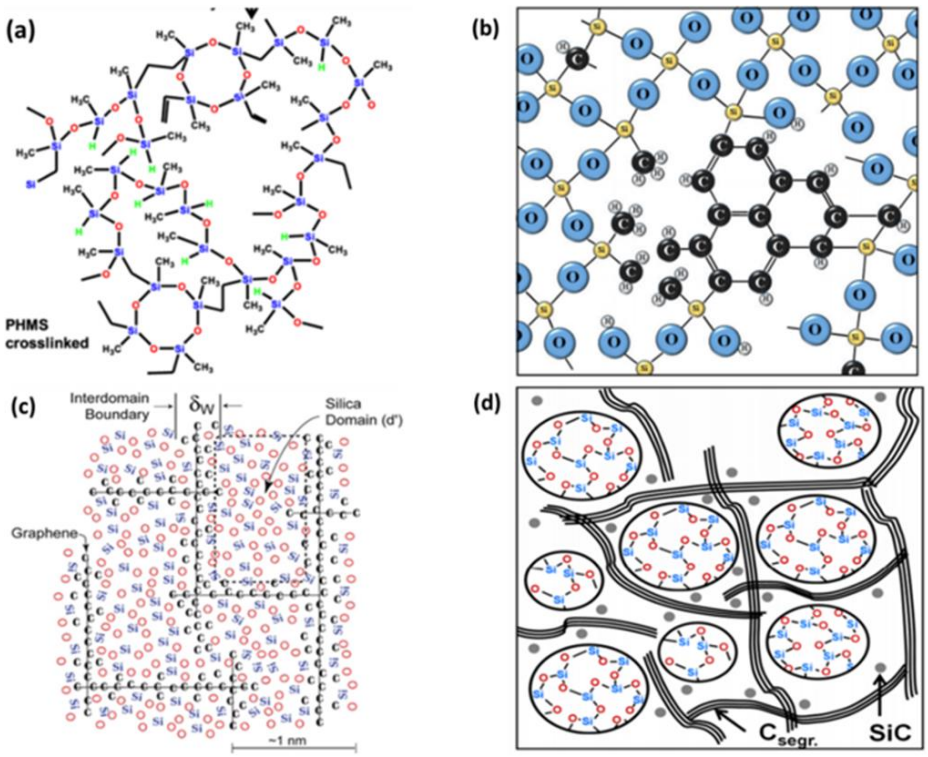

Figure 1. 11. The schematic representations of structural model for (a) crosslinked preceramic polymer, (b) pyrolyzed >600 °C (creamer state) c) pyrolyzed >1000 (glassy state) °C and d) at T >1400 °C (glass-ceramic state). (Sources: Stabler, C., 2019; Stabler, C et. al., 2018)[74, 75]

1.7. Previous Studies about SiOC Spheres Production

The production of spherical SiOC particles, in size of micron and submicron, which are good candidates for many applications such as electronics, sensors, drug delivery, the high-temperature catalyst, filtering, and adsorbing is of significant interest.

Various production methods were used to obtain micron/submicron SiOC spheres. These are micro-fluidization technique[83], electrospraying[84, 85], sol-gel[86-88], and emulsion[66, 77, 78, 89-94] methods. Table 1.1 shows the starting materials, production methods, stirring parameters, and size of micron/submicron SiOC spheres in the literature.

Although the emulsion technique is suitable for the polymer-derived ceramic pathway, few studies have been done on the preparation of submicron SiOC particles.

Additionally, it is seen that the synthesis of submicron SiOC spheres is possible by applying ultrasonication in the emulsion method.

Table 1. 1. Literature review related to the production of submicron/micron SiOC sphere.

Preceramic Polymer	Crosslinker& Catalyst	Method	Stirring	Size of Spheres	Ref.
Polymethylhydrogen Siloxane	DVTMDS TMTVS DVB Pt (0) Karstedt Complex	One-Pot Emulsion	7500-30000 rpm	7-53 µm	[77]
Polymethylhydrogen Siloxane	DVTMDS Pt (0) Karstedt Complex	One-Pot Emulsion	7500 rpm	15.4±6.8 µm	[78]
Polymethylhydrogen Siloxane	DVTMDS TMTVS DVB Pt (0) Karstedt Complex	O/W Emulsion	7500 rpm	19.9-34.6 µm	[89]
Polymethylhydrogen Siloxane	DVTMDS Pt (0) Karstedt Complex	O/W Emulsion	3000 rpm 5000 rpm 7500 rpm 15000 rpm	2 – 40 µm	[94]
Polymethyl Silsesquioxane (MK)	Zirconium (IV) Acetylacetonate	O/W Emulsion	Ultrasonic	~500 nm	[91]
Polymethyl Silsesquioxane (MK)	Zirconium (IV) Acetylacetonate	O/W Emulsion	500 rpm	111±46 µm	[66]
Polymethyl Silsesquioxane (MK)	Zirconium (IV) Acetylacetonate	O/W Emulsion	1000 rpm 20000 rpm Ultrasonic	10–100 µm 1–10 µm 50–600 nm	[93]
Phenyltriethoxysilane Tetraethoxysilane	NA	Sol-Gel	NA	~250 nm	[95]

(Cont. on the next page.)

Table 1.1 (cont.)

Organotriethoxysilane	NA	Stöber Like Synthesis	5000 rpm	100–400 nm	[80]
Methyltrimethoxysilane Dimethyldimethoxysilane	NA	Sol-Gel	NA	3–10 µm	[88]
Triethoxyphenylsilane Tetraethoxysilane	NA	Two-step Sol-Gel	NA	~250 nm	[87]
Phenyltriethoxysilane Methyltriethoxysilane Tetraethoxysilane	NA	Two-step Sol-Gel	NA	~250 nm	[86]
Polymethyl Silsesquioxane (MK)	Zirconium (IV) Acetylacetonate	Micro Fluidization	NA	30 to 180 µm	[83]
Polymethyl Silsesquioxane (MK)	NA	Electrospray	NA	~25–30 µm	[84]
Polymethylphenyl Silsesquioxane	Zinc Acetylacetonate Hydrate	Electrospray	NA	2.5±0.6 µm 3.3±0.8 µm	[85]

In the literature, commercially available polysiloxanes and polysilsesquioxanes (subgroup of polysiloxanes) preceramic polymers were used for the production of SiOC spheres by emulsion technique. Polysiloxanes are inorganic-organic polymers which have Si and O atoms in the main chain. These polymers can have a linear form known as "silicone oil" and highly branched form called "silicone resin" as shown in Figure 1.12.

While polymethylhdyrosiloxane (PHMS) $(CH_3(H)SiO)_n$, in liquid form at room temperature, has –H crosslinking groups, in solid form polymethylsilsesquioxane (MK) $(CH_3O_{1.5}Si)_n$ has –OH and $–OC_2O_5$ crosslinking groups. For curing of linear PHMS preceramic polymer, some crosslinkers, containing vinyl groups (Tetramethylcyclotetrasiloxane: TMTVS and Divinylbenzene: DVB) are used with metal complex (Platinum (Pt) catalyst). Depending on whether there is moisture or water in the

system, there are two types of curing reactions. These are called as hydrosilylation and dehydrocoupling reactions. The crosslinking mechanism is shown in Figure 1.13. With the breaking of double bonds in the crosslinking agent via a catalyst, hydrosilylation reaction takes place by adding the functional hydrogen (Si-H) groups of PHMS and vinyl moieties of TMTVS and DVB each other. So, chemical bonds occur between adjacent chains thanks to the crosslinking agent. As a result, crosslinked (thermoset) structures are obtained. Besides, the dehydrocoupling reaction takes place with the formation of hydrogen gas (H_2) in aqueous systems. So, self-blowing occurs via the release of the H_2 gas.[96-98]

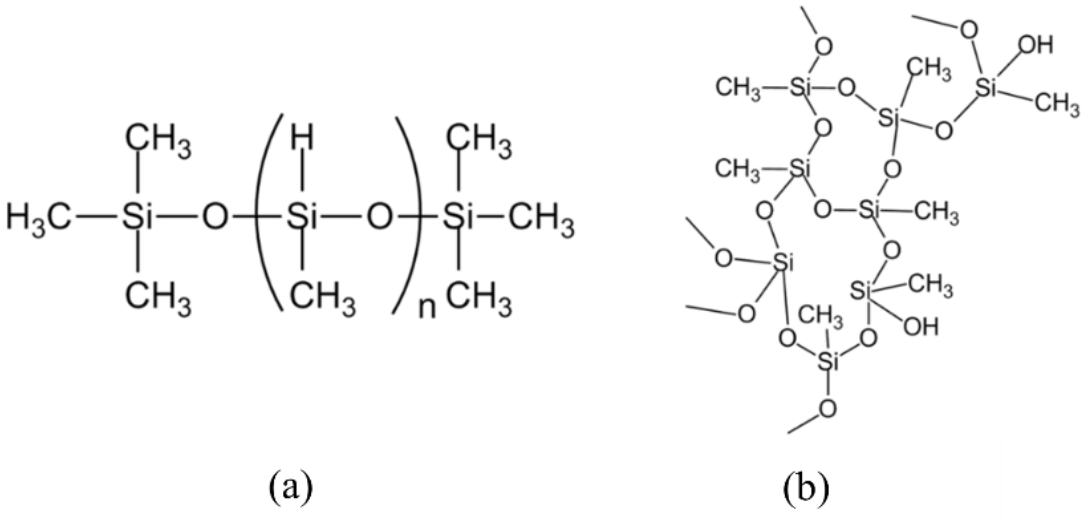

Figure 1. 12. The structure of (a) linear polymethylhdyrosiloxane (PHMS) silicone oil and (b) cage-like form polymethylsilsesquioxane (MK) silicone resin.
(Source: Gelest, 2020, May) [99]

On the other hand, the curing of polymethylsilsesquioxane (MK) resin takes place via a condensation mechanism (shown in Figure 1.14). Some catalysts (e.g. zirconium acetylacetonate, zinc acetylacetonate, and tin catalyst) can be used to accelerate curing at room temperature. At the end of the reaction, water, ethanol, and oligomers may form as the final products.[100]

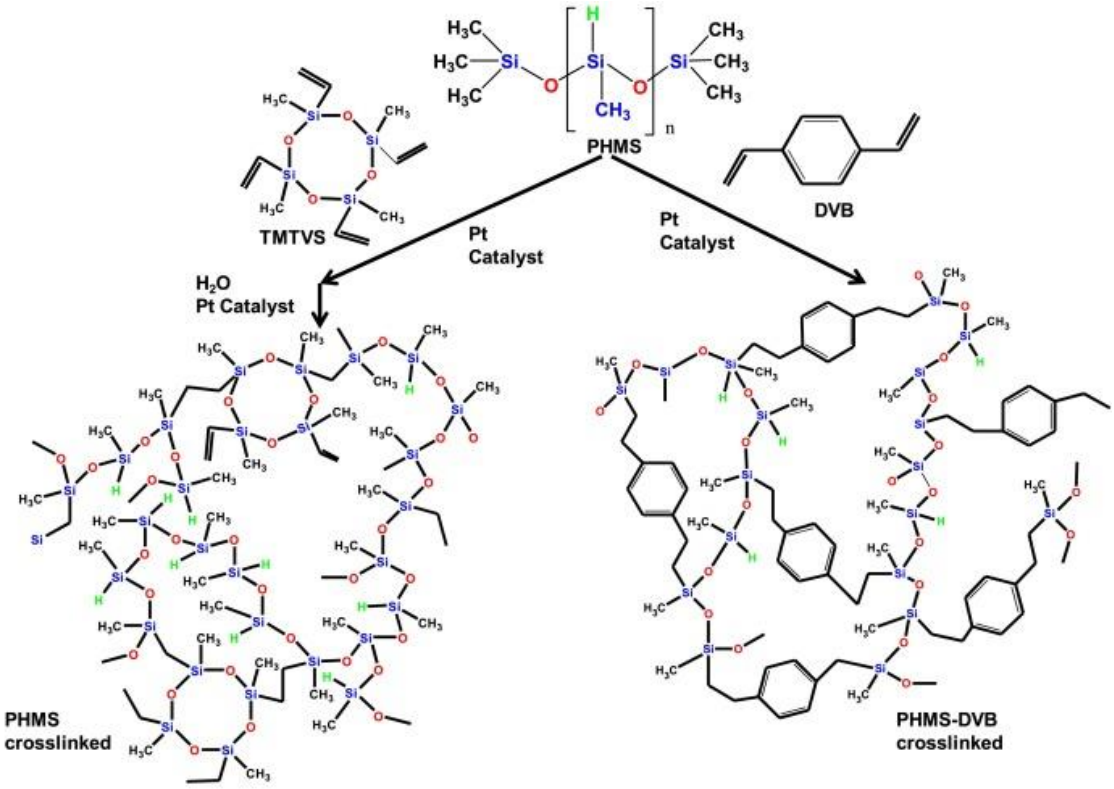

Figure 1. 13. The schematic representation of the curing process of PHMS preceramic polymer.

(Source: Hourlier, D et al.; 2017) [96]

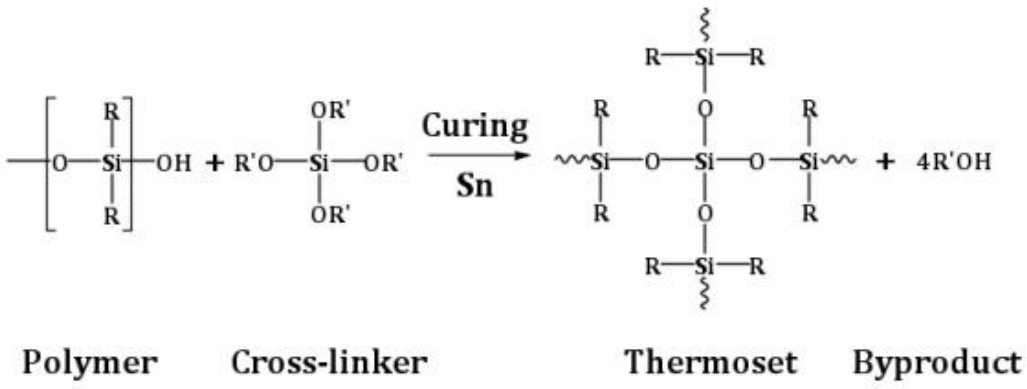

Figure 1. 14. The reaction representation of condensation mechanism.

(Source: Vakifahmetoglu, C., 2010) [63]

After the crosslinking process, thermoset sphere structures are pyrolyzed at different temperatures to obtain SiOC spheres.[77, 78]

In the study that investigated the effect of stirring rates on the sphere size, polysiloxane preceramic polymers (PHMS and DVTMDS) and Pt-catalyst were used as precursors to form SiOC microspheres. Oil and water solution was stirred at different rates (7500 and 30000 rpm) by using a homogenizer. As seen in Figure 1.15, the size of crosslinked polysiloxane spheres was reduced from 26.8 µm to 7.6 µm by increasing the mixing speed.

Figure 1.16 shows the images taken from two different oil in water emulsion studies in the literature. Vakifahmetoglu et al.[66] synthesized SiOC microspheres via o/w emulsion technique. In this study, silicon resin (MK powder), toluene, and zirconium acetylacetonate were used as the oil phase. Also, distilled water (DI) and surfactant (Tween 80) were used as the water phase. The emulsion solution was stirred magnetically at 500 rpm. After curing at 140 ^{o}C, samples were pyrolyzed at 1200 ^{o}C under an inert atmosphere. As a result, SiOC microspheres, having 111±46 µm average particle size and 2.20 m^2/g surface area, were produced (shown in Figure 1.16(a)).

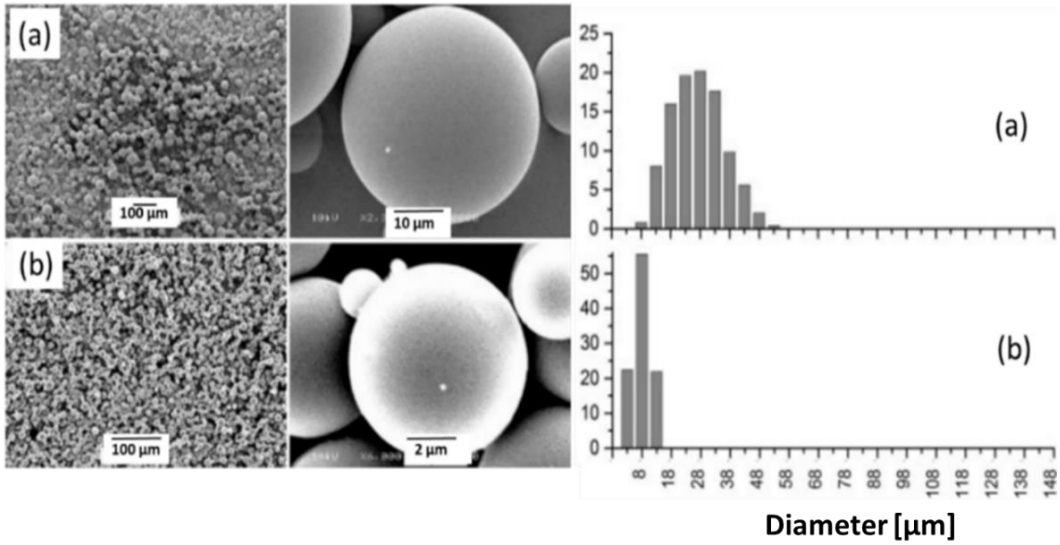

Figure 1. 15. The SEM images and particle size distribution (PSD) plots of crosslinked polysiloxanes microspheres a) stirring at 7500 rpm, (b) stirring at 30000 rpm.

(Source: Fortuniak, W et al.;2016)[77]

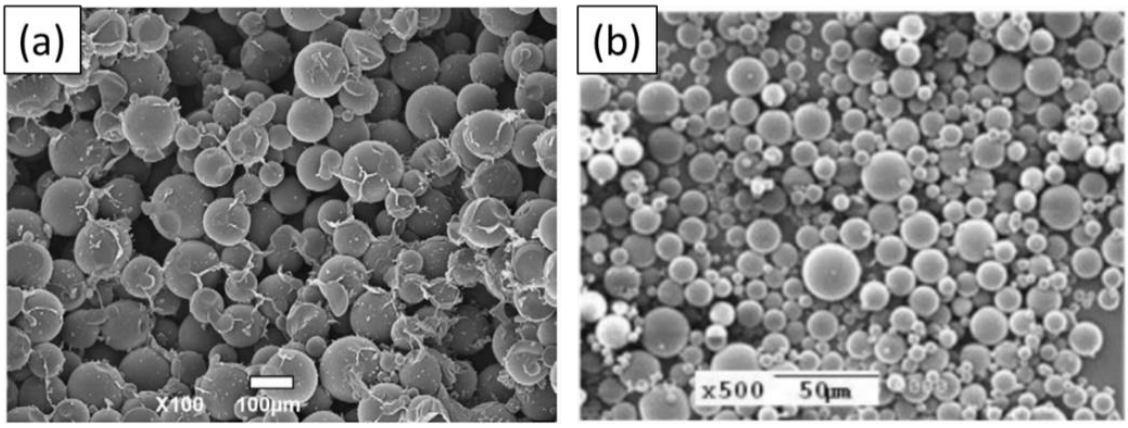

Figure 1. 16. The SEM images of SiOC microspheres produced with o/w emulsion process (a) by magnetic stirring (500 rpm) pyrolyzed at 1200 ^{o}C and (b) by homogenizer stirring (7500 rpm) pyrolyzed at 1000 ^{o}C.

(Sources: Vakifahmetoglu, C et al., 2011[66] and Source:Fortuniak, W et al., 2015[78])

In another study, Fortuniak et al.[78] produced SiOC microspheres by using silicone oil (PHMS), a crosslinking agent (DVTMDS), and catalyst (Pt(0) Karstedt Complex) as oil phase and mixing them at 7500 rpm with homogenizer. Polyvinyl alcohol (PVA) was acted as a surfactant. Crosslinked spheres were pyrolyzed at different temperatures (400-700-1000 ^{o}C). The SEM image of the sample, pyrolyzed at 1000 ^{o}C, is shown in Figure 1.16(b). After pyrolysis at 400 and 1000 ^{o}C, ceramic yields of the samples are 91% and 79%, respectively. Depending on the pyrolysis temperature, at the lower temperature (400 ^{o}C), samples with a high specific surface area (SSA) (278,6 m^2/g) were obtained. With increased pyrolysis temperature (1000 ^{o}C), SSA of samples decreased to 0.8 m^2/g due to the disappearance of micro and mesopores.

In the study[93] on the production of the nanosized (50-600 nm) SiOC spheres by applying the ultrasonication to the emulsion, MK silicone resin, toluene, and zirconium acetylacetonate were used as ceramic precursors. PEO-PPO-PEO block copolymer was used to stabilize the emulsion system. The crosslinking step was carried out in an autoclave. Finally, spheres were pyrolyzed at 1100 ^{o}C under the nitrogen atmosphere. The TEM image of the pyrolyzed samples is given in Figure 1.17.

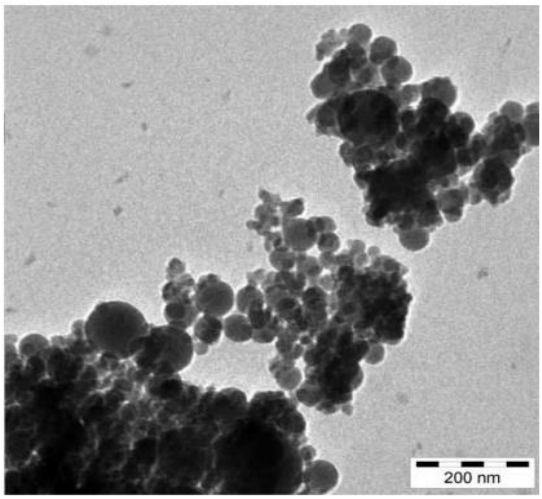

Figure 1. 17. The TEM image of ceramic submicron SiOC spheres produced with the o/w emulsion process by ultrasonically stirring pyrolyzed at 1100 ^{o}C.
(Source: Bakumov, V et al., 2007)[93]

1.8. Photocatalytic Efficiency of SiOC+TiO_2 Materials on Methylene Blue Dye

The photocatalytic activity of SiOC+TiO_2 materials have been investigated in only a few studies.

In the first one of these studies, commeTiO_2 nano-powder was mixed with vinyl-functionalized polysiloxane and pyrolyzed at 700-900 ^{o}C to manufacture mesoporous SiOC+TiO_2 composites. With rising pyrolysis temperature, the surface area of pure SiOC and SiOC+TiO_2 samples decreased by turning of micropores into micro/mesoporosity. The adsorption and photocatalytic performance of the samples were measured with (0.03 mM) MB solution. Among samples pyrolyzed at 700 ^{o}C, mesoporous SiOC/20 wt.% TiO_2 composites exhibited higher photocatalytic activity than pure microporous SiOC ceramic.[101]

In another study[79], PHMS preceramic polymer and Titanium n-tetrabutoxide were used as precursors to synthesis macro and mesoporous SiOC+ TiO_2 nanocomposites. After the formation of TiO_2 nanocrystals (9-10 nm) into amorphous SiOC matrix by pyrolysis at 1200 ^{o}C, photocatalytic performances of samples against 0.03 mM MB solution were investigated. Photodegradation constants of samples were found higher

than the previous study. The photodegradation rate constant values of these studies are given in Table 1.2.

Table 1. 2. The comparison of photodegradation rate constants. (k (min^{-1})

Materials	**k (10^{-3} x min^{-1})**	**MB Concentration (mM)**	**Ref**
SiOC / SiOC+TiO_2	1.3-2.2	0.03	[101]
Macroporous / Microporous SiOC+TiO_2	4.8-3.0	0.03-0.06	[79]

The photo-degradation rate constant (basic kinetic parameter) can be calculated by using the Langmuir Hinshelwood kinetic model[102] Equation (1).

$$\ln(C/C_0) = -kt \qquad (1.1)$$

k: Photo-degradation rate constant

C: Dye concentration instant time (t)

C_0: Initial dye concentration at time (t=0)

CHAPTER 2

EXPERIMENTAL

2.1. Materials and Method

2.1.1. Materials

Two commercially available types of preceramic polymer were used; Trimethylsilyl terminated Polymethylhydrosiloxane (PHMS, Gelest, 30-45 cSt, Mw: 2,100-2,400, CAS: 63148-57-2, USA) and Polymethylsilsesquioxane (Silres MK, Wacker-Chemie GmbH, Germany). Divinylbenzene technical grade 80% (DVB, Merck, CAS: 1321-74-0, Germany) was used as a crosslinking agent for the linear type PHMS preceramic polymer. Platinum-divinyl tetramethyldisiloxane complex in xylene, (2.1-2.4% Pt, abcr GmbH, CAS: 68478-92-2, Germany) and Tin(II) 2-ethylhexanoate (Tin, Sigma- Aldrich, CAS: 301-10-0, USA) were used as catalyst. Polyoxyethylene sorbitan monolaurate (Tween 20, Sigma Aldrich, Mw:1228, USA), Polyoxyethylene sorbitan monooleate (Tween 80, Merck, 300-500 cSt, CAS: 9005-65-6, Germany) and tri-block copolymers of poly(ethylene oxide) poly(propylene oxide)-poly(ethylene oxide) (Pluronic F-127, Sigma Aldrich, CAS: 9003-11-6) were used as the surfactant. As solvent; Acetone (≥ 99.5%, Tekkim, CAS:67-64-1, Turkey), Ethanol (ACS reagent ≥ 99.9%, Merck, CAS:64-17-5, Germany), Xylene (ACS reagent ≥ 99.8%, Merck, CAS:1330-20-7, Germany), Toluene (ACS reagent ≥ 99.9%, Merck, CAS: 108-88-3, Germany), and deionized (DI) water were used. Titanium(IV) n-butoxide (TNBT, 99+%, Alfa Aesar, CAS: 5593-70-4, Germany) was used as a source for anatase phase titanium dioxide.

2.1.2. Equipment

Magnetic stirrer and ultrasonic probe sonicator (QSonica) were used for the mixing of emulsion solution. Tube furnace (Protherm, Model: PTF 16/75/450, Ankara, Turkey) and elevating furnace (Protherm) were used for the heat-treatment of samples. UV lamp (300 Watt, 280-400 nm, Osram UV lamp) cabin system was designed and made for photocatalytic experiments.

2.1.2.1. Design and Manufacturing of UV Lamp Cabin

The designed UV lamp cabin system was manufactured by the Metal Studio at the IZTECH. Cabin has 40 cm*40 cm*70 cm dimensions. Eight fans were used to cool the cabin that became warm due to the UV lamp. Three of these fans are located in the upper part, two in the middle and three in the bottom part on the left and right side of the cabin. A metal sheet (1 mm thickness) was used in the construction of the cabin scaffold. The inside of the cabin was covered with aluminum foil for reflection of ultraviolet rays. 2D drawings of the UV lamp cabin system are shown in Figure 2.1. And also, 3D drawings and photographs are shown in 2.2.

Figure 2. 1. The 3D Autocad drawings (a & b), and the photographs of UV lamp cabin system (c & d).

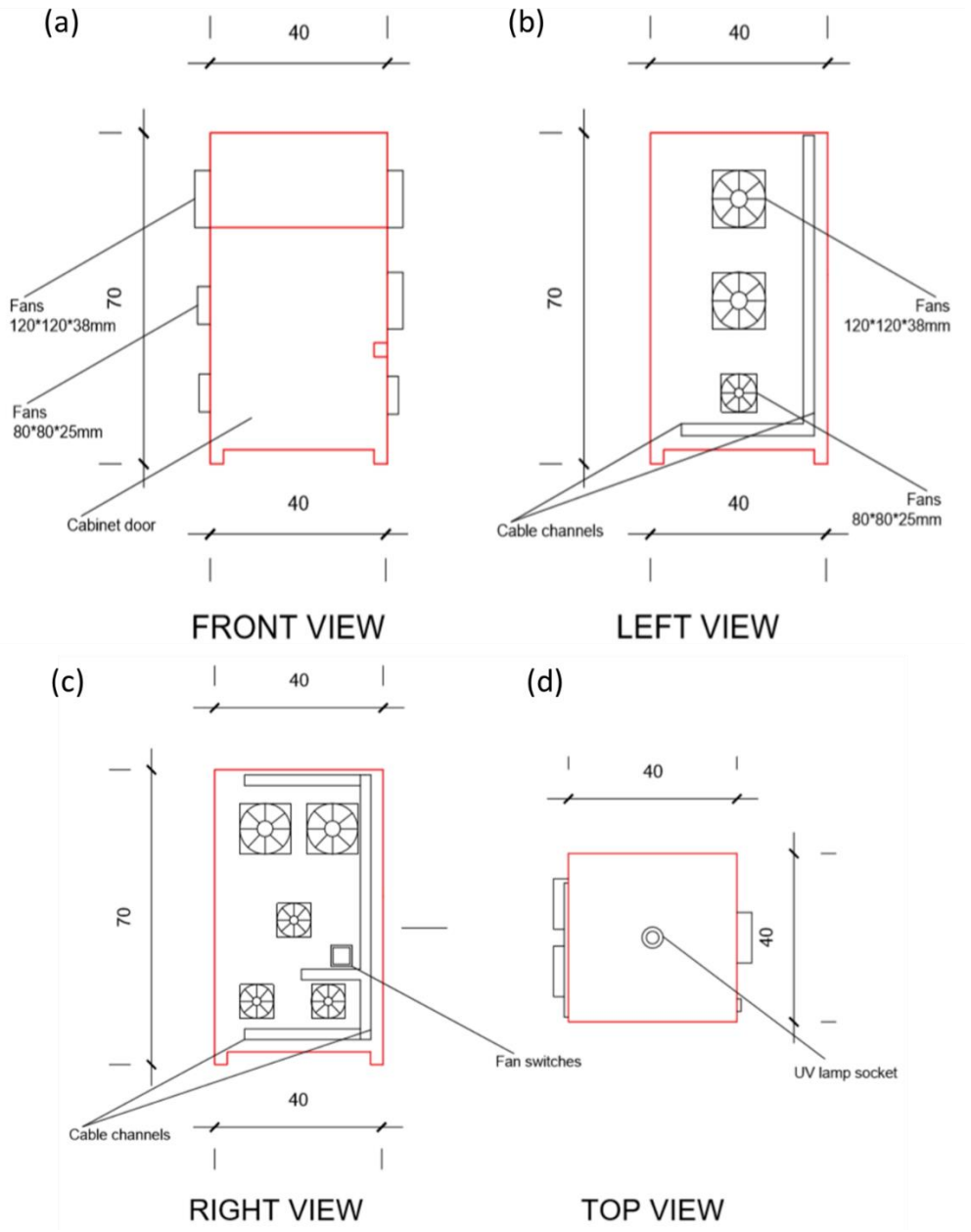

Figure 2. 2. The Autocad drawings of UV Lamp Cabin (a) front view, (b) left view, (c) right view, and (d) top view.

2.1.3. Production of SiOC Spheres from Silicone Oil

Procedure 1: Firstly, 10 ml of distilled (DI) water and 0.15 grams of surfactant (Tween 20) were mixed by magnetic stirrer at 1500 rpm for 15 minutes in a beaker. In another beaker, preceramic polymer (2 grams of PHMS) and crosslinking agent (200 µl

of DVB) were mixed at 250 rpm for 5 minutes. Then 0.05% diluted Pt catalyst in xylene (200 µl of Pt Catalyst Complex) was added to the oil phase and mixed 1 more minute. The oil phase was added drop by manner into the water phase solution and mixed by applying ultrasonic probe sonicator (with 20% Amplitude) for 1 min. The curing process was conducted at R.T for 24 h.

Procedure 2: Firstly, 10 ml of distilled (DI) water and 0.15 grams of surfactant (Tween 20) were mixed by magnetic stirrer at 1500 rpm for 15 minutes in a beaker. Secondly, preceramic polymer (2 grams of PHMS) was added drop by manner into the water phase solution and stirred for 10 minutes. Then oil in water emulsion solution was mixed by applying ultrasonic probe sonicator for 5 min. Crosslinking agent (200 µl of DVB) and catalyst (Pt Catalyst Complex) were added in order and mixed 1 more minute. After the milky emulsion solution was obtained, the curing process was conducted at 80 ^{o}C for 24 h and at 150 ^{o}C for 8 h, respectively. After the curing process, samples were grounded in the mortar. Finally, cured samples were pyrolyzed at 1000 ^{o}C (heating rate: 2 ^{o}C/min and dwell time: 2h) in a tube furnace under inert (Ar) atmosphere.

The order of catalyst addition to preceramic blend, the amplitude of the ultrasonic probe, and the effect of Pt-Catalyst amount were used as parameters to change the particle size of spheres. The sample codes and production parameters are given in Table 2.1

In Table 2.1, samples were named as follows; U: Ultrasonic probe sonicator, P: PHMS preceramic polymer.

Table 2. 1. The production parameters of oil in water (Preceramic polymer blend (PHMS+DVB+Pt Catalyst) / DI water) emulsion systems.

Sample Codes	**Catalyst Addition**	**Pt Catalyst (µl)**	**Stirring (Rate and Type)**
UP1	Before sonication	200	20% Amplitude (Sonicator)
UP2	After sonication	200	20% Amplitude (Sonicator)
UP3	After sonication	200	30% Amplitude (Sonicator)
UP4	After sonication	200	50% Amplitude (Sonicator)

(Cont. on the next page.)

UP5	After sonication	400	20% Amplitude (Sonicator)
UP6	After sonication	600	20% Amplitude (Sonicator)

2.1.4. Production of SiOC Spheres from Silicone Resin

Firstly, 80 ml of distilled (DI) water and 0.8 grams of surfactant (Pluronic F127) were mixed by magnetic stirrer at 500 rpm for 20 minutes in a beaker. In another beaker, 5 grams of preceramic polymer (MK powder) and 7 ml of solvent (Toluene) were mixed as oil phase at 500 rpm for 10 minutes. The oil phase was added drop by manner into the water phase solution and stirred for 30 minutes. Then, the o/w emulsion solution was mixed in the ice bath by applying an ultrasonic probe sonicator (with 50% Amplitude) for 5 min. 500 µl of catalyst (15 vol.% Tin catalyst in xylene) were added and mixed 3 more minutes. After the milky emulsion solution was obtained, the curing process was carried out for 18 h by heating from room temperature to 140 °C. Additionally, one sample was produced by only magnetically stirring for comparison with stirred samples via the ultrasonic probe. After the curing process, samples were grounded in the mortar. Finally, cured samples were pyrolyzed at different temperatures (600-800-1000, and 1200 ^{o}C) in a tube furnace under inert (Ar) atmosphere (heating rate: 2 ^{o}C/min and dwell time: 2h)

Table 2. 2. The production parameters of oil in water (MK/DI water) emulsion systems.

Sample Codes	**Stirring (Rate and Type)**	**Pyrolysis Temperatures/ Atmosphere/Time**
MM1000	500 rpm (Magnetic Stirrer)	1000 ^{o}C /Ar/2h
UM600	50% Amplitude (Sonicator)	600 ^{o}C/Ar/2h
UM800	50% Amplitude (Sonicator)	800 ^{o}C /Ar/2h
UM1000	50% Amplitude (Sonicator)	1000 ^{o}C/Ar/2h
UM1200	50% Amplitude (Sonicator)	1200 ^{o}C /Ar/2h

In Table 2.2, samples were named as follows; M: Magnetic stirrer, U: Ultrasonic probe sonicator and M: MK preceramic polymer and pyrolysis temperatures.

2.1.5. Production of TiO_2 Coated SiOC Submicron/Nanospheres

Titanium(IV) n-butoxide/ethanol solution, with different molarities (0.01 M, 0.03 M and 0.06 M), were prepared as titanium precursor. In the previous step produced MK derived SiOC samples (0.4 g) were impregnated with titanium dioxide precursor solutions for 24 h at R.T by stirring at 200 rpm. At the end of the mixing, samples were degassed with an ultrasonic bath for 30 minutes to ensure that titanium solution penetration into samples successfully. Then samples were dried at 80 ^oC in the oven to remove the solvent. After drying, samples were heat-treated at 450 ^oC for 4 h to obtain anatase phase TiO_2. Production parameters of TiO_2 coated SiOC samples were shown in Table 2.3. The samples were coded assuming that SiOC substrates coated theoretically with 5%, %10, and 20% TiO_2.

Table 2. 3. TiO_2 coated SiOC samples and their production properties.

Sample Codes	TiO_2 Content (%)	Pyrolysis Temperatures (^oC)
UM600T5	5	600
UM600T10	10	600
UM600T20	20	600
UM800T5	5	800
UM800T10	10	800
UM800T20	20	800
UM1000T5	5	1000
UM1000T10	10	1000
UM1000T20	20	1000

(Cont. on the next page.)

UM1200T5	5	1200
UM1200T10	10	1200
UM1200T20	20	1200

2.2. Characterization

The morphological characterization of samples, after both curing and pyrolysis processes, were analyzed by Optical Microscopy (Olympus BX53 Upright), Scanning Electron Microscopy (SEM; FEI Quanta 250 FEG). Before SEM analysis, the surface of the samples was coated with a thickness of ~10 nm of Au. The size of the spheres was measured from SEM images by using the Image J program (200 measurements for each sample). Phase analysis of the powders was carried out with the X-ray Diffraction (Philips X'Pert Pro instrument; 2θ;10˚-90˚and the scan step; 0.005 ˚/second). Fourier transform infrared spectra (FTIR) were recorded (Perkin Elmer FTIR Spectrum 100) in the range 450-4000 cm^{-1}. Thermogravimetric analysis was conducted to show the thermal stabilities of samples, by heating from RT to 1200˚C with a 5˚C/min^{-1} heating rate in air atmospheres. Nitrogen (N_2) gas adsorption analyses were conducted on samples pyrolyzed at different temperatures. The isotherms were collected using Gemini V (Micrometirics**)** instrument. The samples were firstly degassed at 200 ºC for 12 h before analysis. Specific surface area (SSA) was determined from a BET (Brunauer–Emmett–Teller) analysis. Also, pore size distributions were obtained from the desorption part of the isotherm. Photocatalytic performance measurements were conducted by using UV2550 (SHIMADZU) Ultraviolet-visible (UV-Vis) spectrophotometer.

CHAPTER 3

RESULTS AND DISCUSSION

3.1. Morphological Characterization of Spheres Derived from Silicone Oil

The morphologies of samples derived from PHMS preceramic polymer via o/w emulsion method were analyzed by Optical Microscopy (OM) and Scanning Electron Microscopy (SEM).

Figure 3.1 demonstrates images taken by optical microscopy of the sample produced by oil in water emulsion method (Procedure 1). Briefly, in procedure 1, distilled (DI) water and surfactant were mixed by a magnetic stirrer. In another beaker, preceramic polymer (PHMS) and crosslinking agent (DVB) were mixed. Then catalyst (Pt Catalyst Complex) was added to the oil phase and mixed 1 more minute. The oil phase was added drop by manner into the water phase solution and mixed by applying ultrasonic probe sonicator (with 20% Amplitude) for 1 min. So, the addition of the catalyst was performed before mixing with an ultrasonic probe sonicator. The samples were cured at R.T for 24 h.

As seen in Figure 3.1, the sizes of cured spheres are in the micron size. It is seen that the size of the spheres increases after curing compared to after emulsification. It can be explained by the coalescence of the oil droplets in the emulsion system.[103]

Optical microscopy and SEM images of samples produced by oil in water emulsion method (Procedure 1 & 2) are shown in Figure 3.2.

Briefly, in procedure 2, distilled (DI) water and surfactant were mixed by a magnetic stirrer. Then, preceramic polymer (PHMS) was added drop by manner into the water phase solution and stirred for 10 minutes. Then oil in water emulsion solution was mixed by applying ultrasonic probe sonicator for 5 min. Crosslinking agent (DVB) and catalyst (Pt Catalyst Complex) were added in order and mixed 1 more minute. So, adding of curing agent and catalyst to preceramic polymer was conducted after mixing with an

ultrasonic probe sonicator. After the milky emulsion solution was obtained, samples were cured at 80 ˚C for 24 h and 150 ˚C for 8 h, respectively.

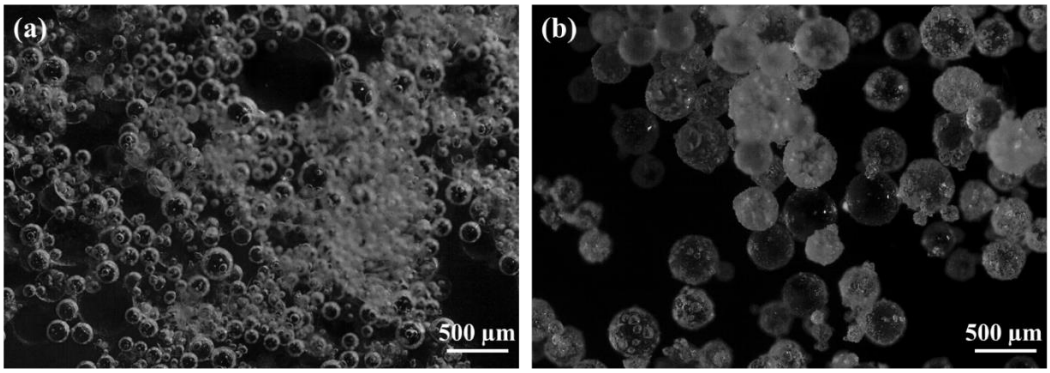

Figure 3. 1. The optical microscopy (OM) images of the UP1 sample prepared by o/w emulsion system (Oil phase; PHMS: 2 g + DVB: 200µL + Pt Catalyst: 200 µL) / Water phase; DI water: 10 ml and surfactant: 0.15 g); (a) immediately after the emulsification via ultrasonic probe (with a %20 amplitude), and (b) after curing for 24 h at R.T.

As seen in Figure 3.2, the samples (UP1) in which the catalyst was added before ultrasonic mixing are larger than ones (UP2) the catalyst was added later.

Also, size measurements of spheres were made using the Image J program from SEM images. The data (diameter of the circle) obtained by Image J measurements is 2 dimensional. Stereological equation $D_{sphere}=D_{circle}/0.785$[66, 104] was applied to convert 2D measurements to 3D values. The particle size distribution (PSD) plots were obtained from 3D (diameter of the spheres) values.

Figure 3.3 display the PSD plots of UP1 and UP2 samples. The average size was calculated 513±81 µm and 0.52±0.28 µm, respectively. According to SEM images and PSD plots, catalyst addition before sonication probably caused the curing of the preceramic polymer. Therefore, sonicator could not make smaller spheres because of cured preceramic structure. But, catalyst addition after sonication made submicron/nano preceramic polymer spheres in the emulsion system cure.

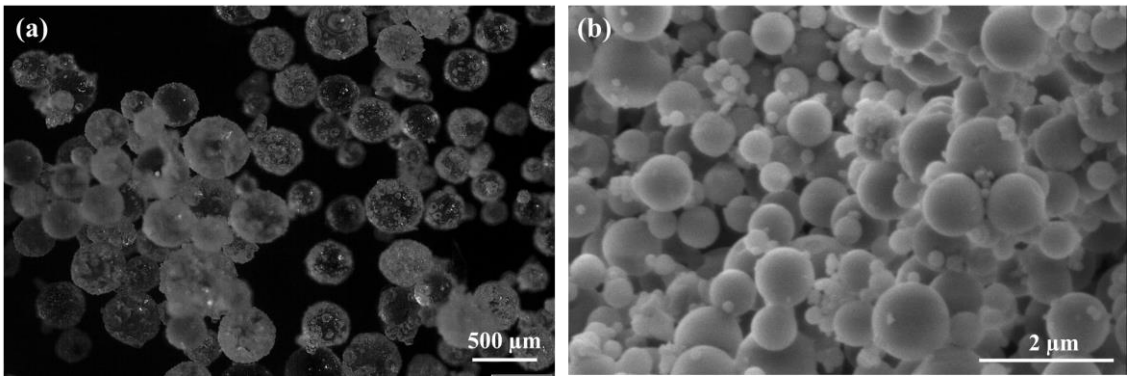

Figure 3. 2. Images of the samples (after curing) prepared by o/w emulsion system (Oil phase; PHMS: 2 g + DVB: 200µL + Pt Catalyst: 200 µL) / Water phase; DI water: 10 ml and surfactant: 0.15 g); (a) The OM image of the UP1 sample (catalyst addition before sonication with a %20 amplitude), and (b) SEM image of UP2 sample (catalyst addition after sonication with a %20 amplitude).

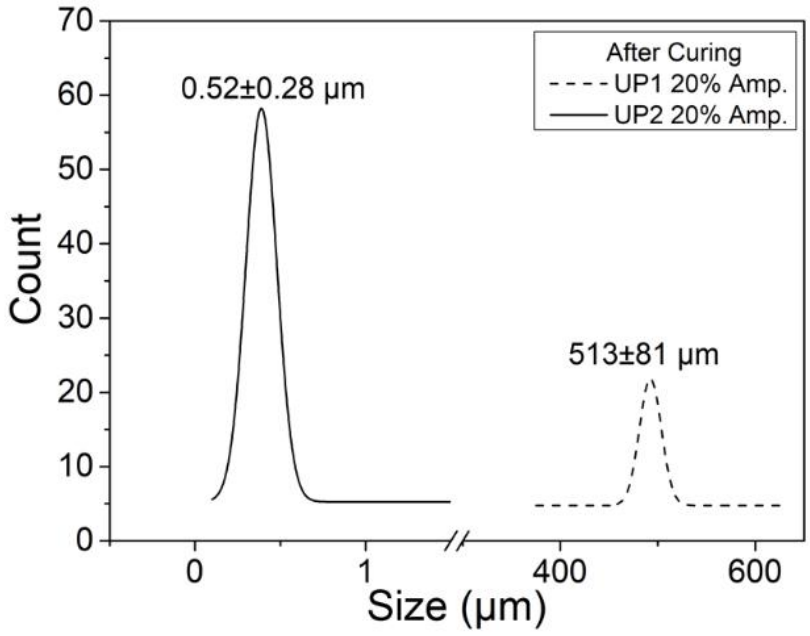

Figure 3. 3. The PSD plots of cured UP1 sample (catalyst addition before sonication with a %20 amplitude) and UP2 sample (catalyst addition after sonication with a %20 amplitude).

After obtaining submicron spheres by the addition of the crosslinker and catalyst following mixing by sonication, different amplitude values of the ultrasonic probe sonicator were studied as spheres size reduction parameter. Following the curing process, samples were grounded in the mortar. Finally, cured samples were pyrolyzed at 1000 ^{o}C (heating rate: 2 ^{o}C/min and dwell time: 2h) in a tube furnace under inert (Ar) atmosphere.

Figure 3.4 shows the SEM images of the samples produced via o/w emulsion method by ultrasonic probe sonicator with different amplitude values (20-30-50% Amp).

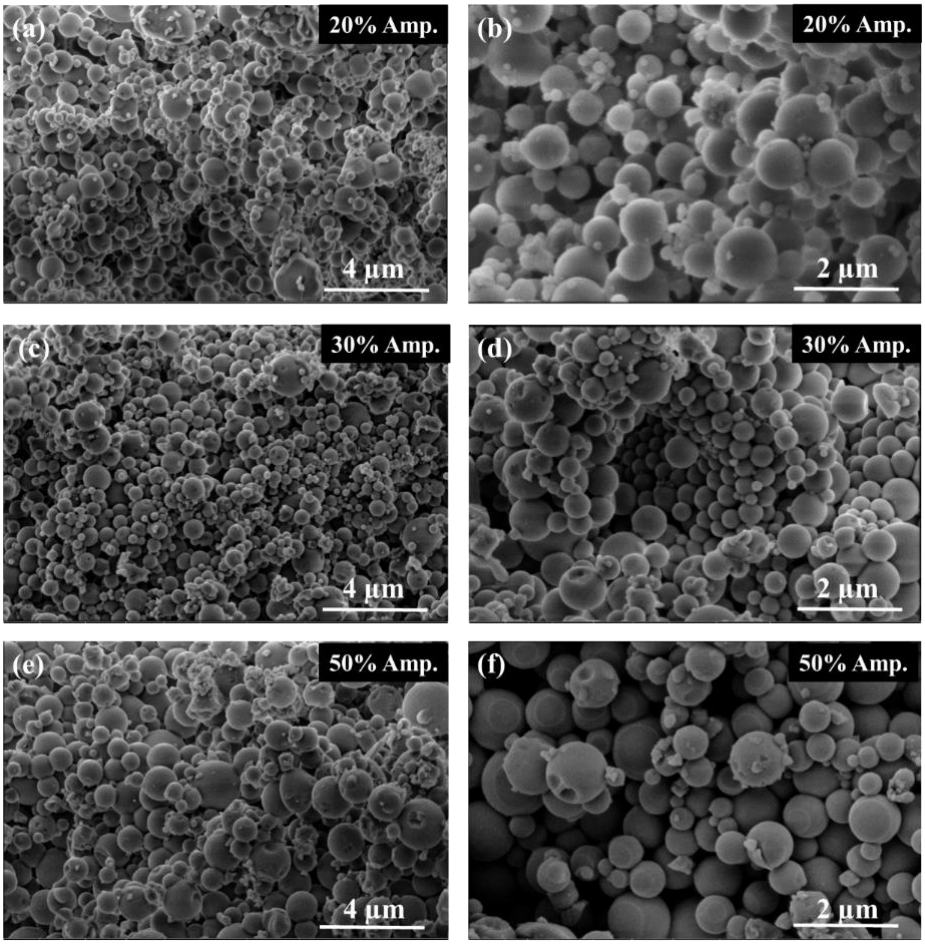

Figure 3. 4. The SEM images of the samples prepared by o/w emulsion system (Oil phase; PHMS: 2 g + DVB: 200µL + Pt Catalyst: 200 µL) / Water phase; DI water: 10 ml and surfactant: 0.15 g) after curing; (a) UP2: 20% Amp., (c) UP3: 30% Amp., (e) UP4: 50% Amp. and after pyrolysis at 1000 ^{o}C for 2h under Ar atmosphere; (b) UP2, (d) UP3, (f) UP4. (For all samples catalyst addition after sonication)

Figure 3.5 shows the PDS plots of samples that are mixed with different amplitudes by the ultrasonic probe sonicator. After curing, the average sphere size of the samples mixed with 20%, 30%, and 50% amplitudes are 521±277, 714±263, and 1266±447 nm, respectively. The size of the spheres increased with rising amplitude values. It might be due to the following reason. While mixing of emulsion solution by sonicator with higher amplitude values, excess heat was generated. Sonicators produce the sound waves with alternating cycles of compression and expansion, with rates depending on the sound wave frequencies. So, the curing step of preceramic polymer spheres probably occurred at the expansion cycle because of the increasing temperature of the emulsion solution.

Following the pyrolysis of the samples, the size of spheres decreased due to some volumetric shrinkage during ceramization. But, spherical structures were not changed and no crack was seen. SiOC samples produced mixing with 20%, 30%, and 50% amplitudes have average sphere size 410±242, 775±322, and 952±302 nm, respectively.

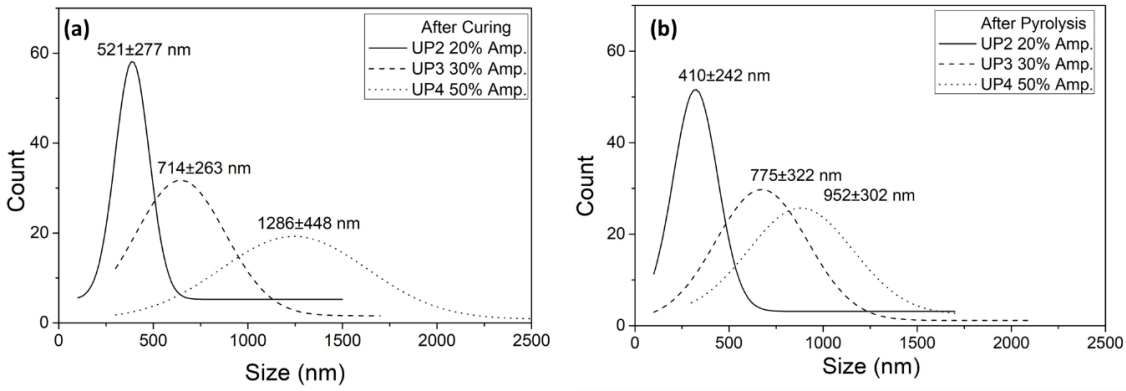

Figure 3. 5. The PSD plots of samples prepared by sonicating with different amplitudes UP2: 20% Amp., UP3: 30% Amp. and UP4: 50% Amp.; (a) after curing at 80 ^{o}C for 24 h and 150 ^{o}C for 8 h, respectively, and (b) after pyrolysis at 1000 ^{o}C for 2h under Ar atmosphere.

On the other hand, the amount of Pt-Catalyst complex was studied as a parameter in the obtaining of polymeric spheres. The SEM images of the samples produced by

adding different amounts of catalyst complex are shown in Figure 3.6. It was seen non-spherical particles among spheres obtained using 400 and 600 µL of catalyst.

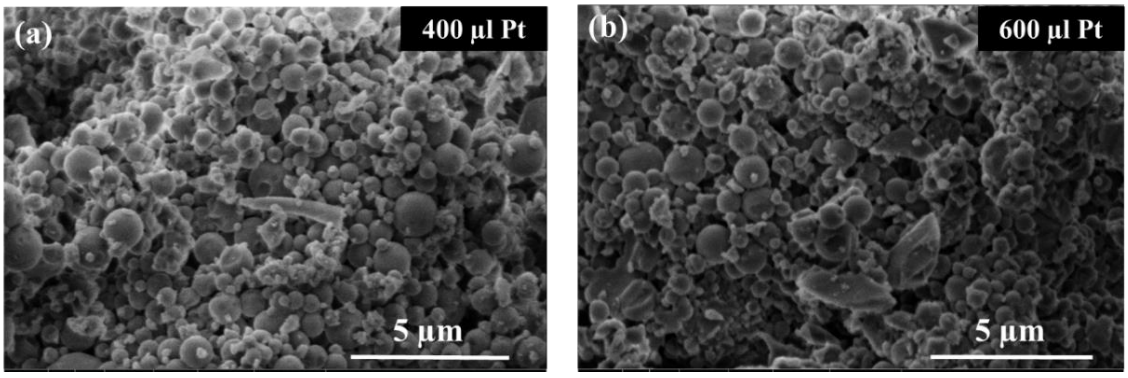

Figure 3. 6. The SEM images of the samples (after curing at 80 ºC for 24 h and 150 ºC for 8 h, respectively) produced via o/w emulsion system (Oil phase; PHMS: 2 g + DVB: 200 µL + Pt Catalyst:400-600 µL) / Water phase; DI water: 10 ml and surfactant: 0.15 g); (a) UP5 (catalyst: 400 µL) and (b) UP6 (catalyst: 600 µL).

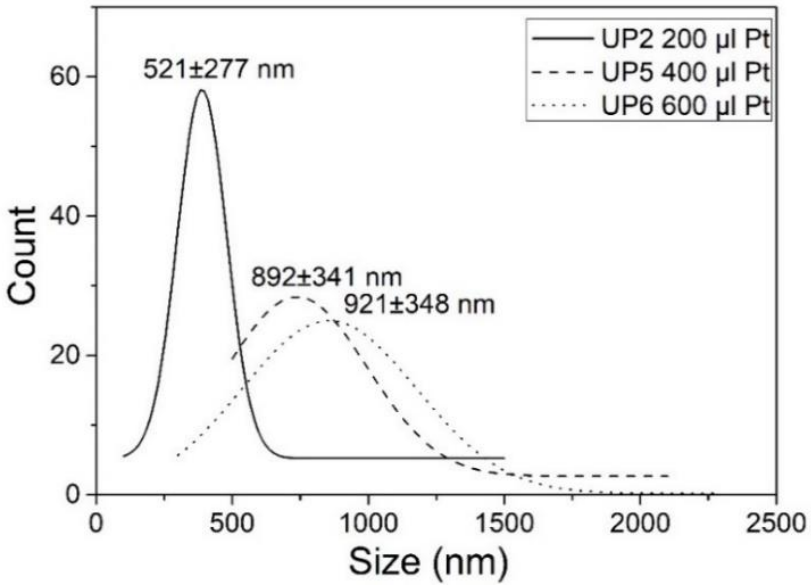

Figure 3. 7. The PSD plots of samples produced by adding different amounts of Pt catalyst complex; UP2 (200 µL), UP5 (400 µL), and UP6 (600 µL).

The effect of catalyst amount on particle size is shown in Figure 3.7. By increasing the amount of catalyst complex to 3 times, the size of spheres almost doubled (from 521±277 to 921±348 nm). Increasing in size can be possibly explained by occurring of curing quickly during mixing with the sonicator.

3.2. Structural Characterization of Spheres Derived from Silicone Oil

FTIR spectra were taken from the cured and pyrolyzed samples are shown in Figure 3.8. In the spectra for pure polymethylhydrosiloxane (PHMS) polymer and cured samples, the absorption of the characteristic Si-CH_3 bond located around 756, 1259, and 2965[66, 105, 106] cm^{-1} is clearly seen from Figure 3.8(a). The typical vibration Si-O-Si band at 1035 cm^{-1} came from the backbone of PHMS.

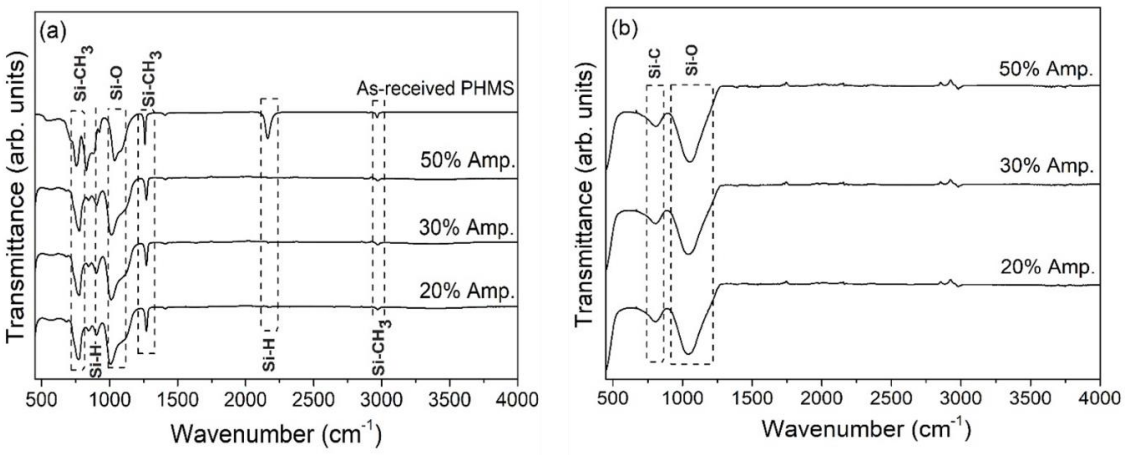

Figure 3. 8. The FTIR spectra of samples prepared by sonicating with different amplitudes UP2: 20% Amp., UP3: 30% Amp. and UP4: 50% Amp (a) after curing and (b) after pyrolysis at 1000 ˚C for 2h under Ar atmosphere.

After curing, the strong intensity of the Si–H absorption band at 2160 cm^{-1} in the starting precursor (PHMS) disappeared. This change is a sign of the occurring of hydrosilylation reaction between vinyl groups of DVB and Si – H group of PHMS.[106] As a result, it can be said that curing has taken place successfully.

The spectra recorded for samples pyrolyzed at 1000 °C are shown in Figure 3.8(b). Evidence of the SiOC ceramic structure formation is indicated by Si-C stretching peak centering 805 cm^{-1}, and also broad peak centering ~1050 cm^{-1}, corresponding Si-O stretching in Si-O-Si or Si-O-C.[107 108]

Figure 3.9 shows the XRD pattern of UP2 sample pyrolyzed at 1000 °C. Broad peaks between 10° and 30° range (2θ) indicate the characteristics of amorphous SiOC materials.

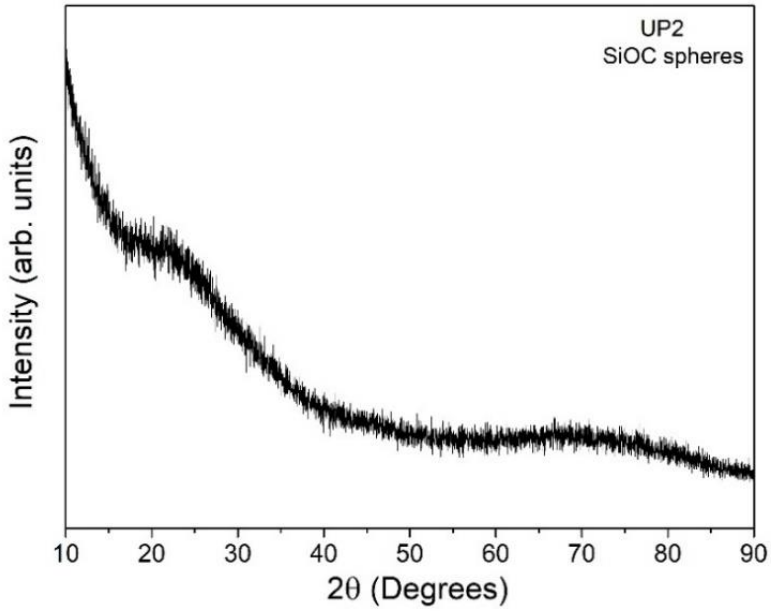

Figure 3. 9. XRD pattern of (UP2: 20% Amp.) sample pyrolyzed sample at 1000 °C for 2h under Ar atmosphere.

3.3. Morphological Characterization of Spheres Derived from Silicone Resin

Morphologies of samples derived from MK preceramic polymer via o/w emulsion method were analyzed by SEM.

Figure 3.10 shows the SEM images of the sample (MM1000) produced via o/w emulsion method using a magnetic stirrer. Briefly, distilled (DI) water and surfactant were

mixed by magnetic stirrer at 500 rpm for 20 minutes in a beaker. In another beaker, preceramic polymer (MK powder) and solvent (Toluene) were mixed as oil phase at 500 rpm for 10 minutes. Then, the oil phase was added drop by manner into the water phase solution and stirred for 30 minutes. 500 µl of catalyst (15 vol.% Tin catalyst in xylene) was added and mixed 15 more minutes. The emulsion system was cured for 18 h by heating from room temperature to 140 °C. After the curing process, samples were grounded in the mortar and pyrolyzed in a tube furnace (at 1000 $^{\circ}$C, 2 $^{\circ}$C/min heating rate, and 2h dwell time/ under (Ar) atmosphere.

It can be seen that from SEM images of MM1000 sample, produced by magnetically stirred, the size of cured spheres around hundreds of micron sizes. After pyrolysis, spheres agglomerated and seen in Figure 3.10(b).

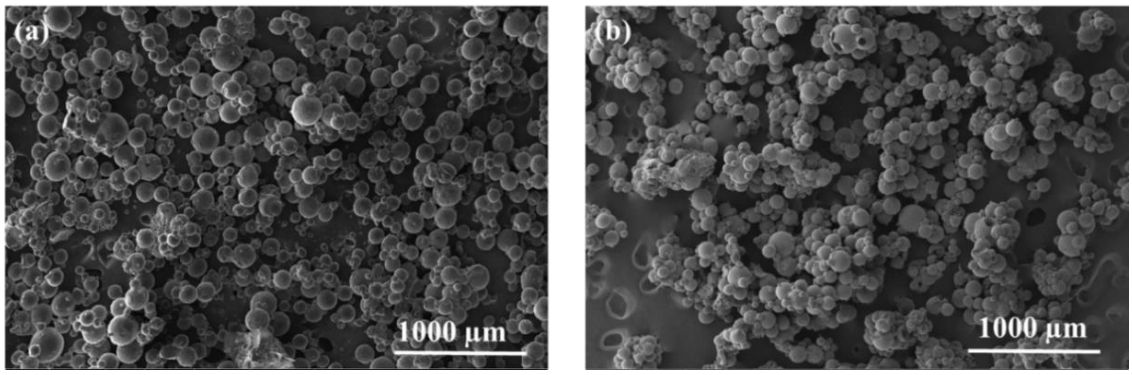

Figure 3. 10. The SEM images of the samples produced via o/w emulsion system by magnetically stirring (Oil phase; MK resin: 5 g + Toluene:7 mL+ Tin Catalyst: 500 µL) / Water phase; DI water: 80 ml and surfactant: 0.8 g); (a) sample (MM) after curing at 140 ^{o}C for 18h, and (b) sample (MM1000) after pyrolysis at 1000 ^{o}C for 2h under Ar atmosphere.

Figure 3.11 shows PSD of samples after curing and pyrolysis. After curing and pyrolysis, the size of the samples is 151±51 µm and 112±45 µm, respectively.

Figure 3.12 shows the SEM images of the cured samples produced via o/w emulsion method by applying an ultrasonic probe sonicator. Initially, distilled (DI) water and surfactant were mixed by magnetic stirrer at 500 rpm for 20 minutes in a beaker. In

another beaker, preceramic polymer (MK powder) and solvent (Toluene) were mixed as oil phase at 500 rpm for 10 minutes. Then, the oil phase was added drop by manner into the water phase solution and stirred for 30 minutes. Then o/w emulsion solution was mixed in the ice bath by applying an ultrasonic probe sonicator with 50% amplitude for 5 min. 500 µl of catalyst (15 vol.% Tin catalyst in xylene) was added and mixed 3 more minutes. The emulsion system was cured for 18 h by heating from room temperature to 140 °C. After the curing process, samples were grounded in the mortar. Finally, cured samples were pyrolyzed at 600-800-1000 and 1200 °C temperatures in a tube furnace under (Ar) atmosphere. The cause of the pyrolysis at lower temperatures is to obtain transient porosity.

When compared to samples produced with a magnetic stirrer, it is seen that samples produced with ultrasonic probe sonicator are homogeneous nano/submicron size.

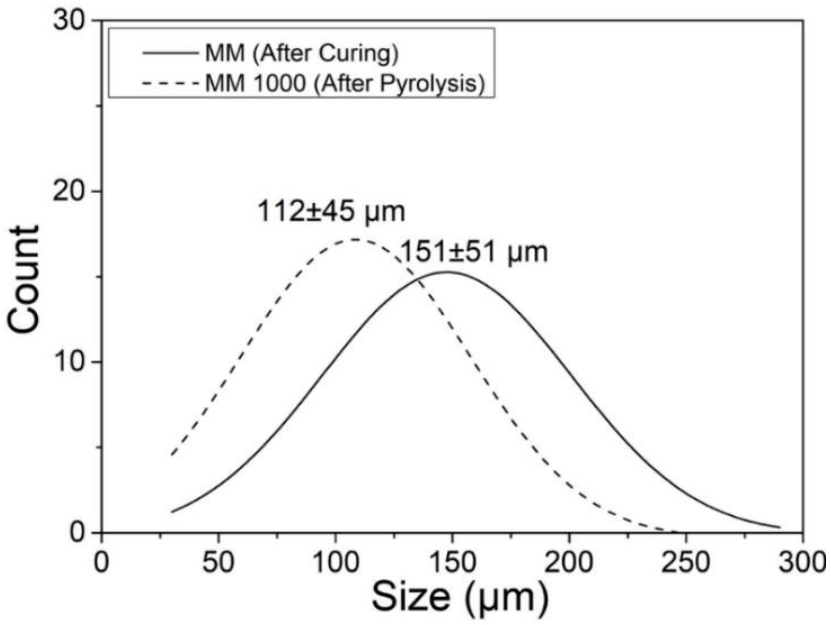

Figure 3. 11. The PSD plots of MM; cured at 140 ºC, 18h, and MM1000 sample; pyrolyzed at 1000 ºC for 2h under Ar atmosphere.

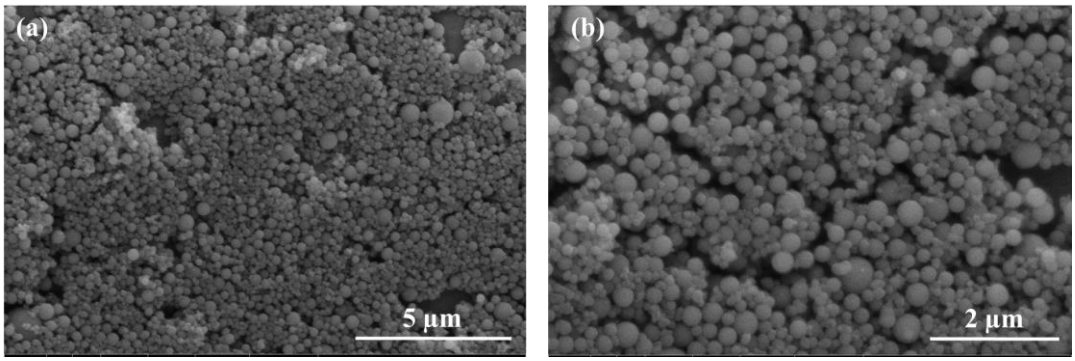

Figure 3. 12. The SEM images of the UM samples (after curing at 140 ºC for 18h) produced via o/w emulsion system stirred ultrasonically with 50% Amp. (Oil phase; MK resin: 5 g + Toluene:7 mL+ Tin Catalyst: 500 µL) / Water phase; DI water: 80 ml and surfactant: 0.8 g) (a) general and (b) higher magnification view.

SEM images of the pyrolyzed (at 600-800-1000-1200 ºC) samples are shown in Figure 3.13. In addition, particle size distributions obtained from SEM images of cured and pyrolyzed samples are shown in Figure 3.14.

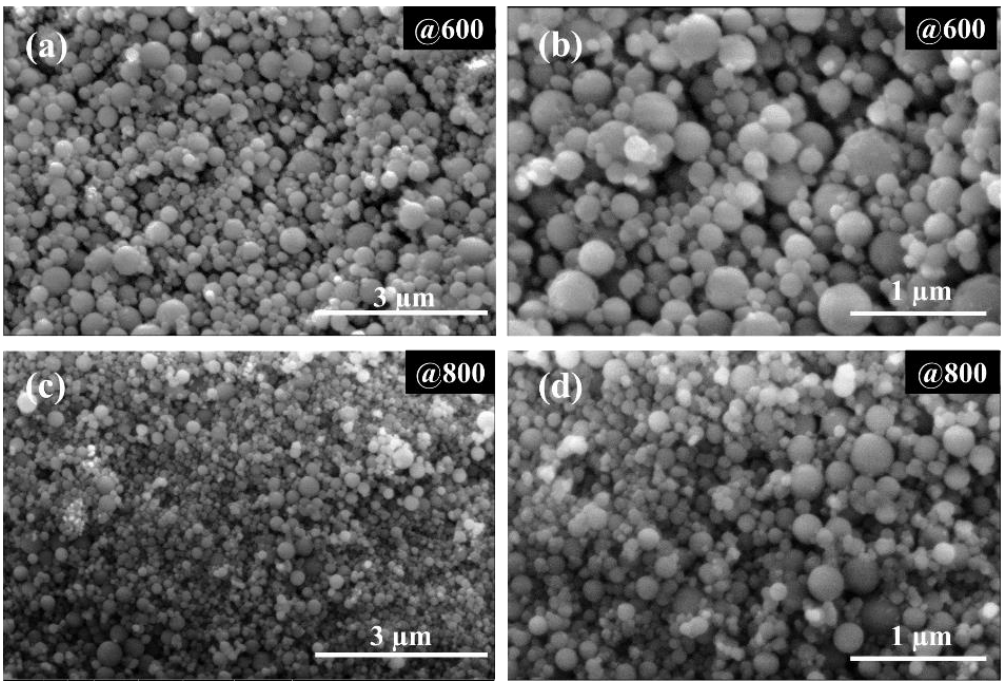

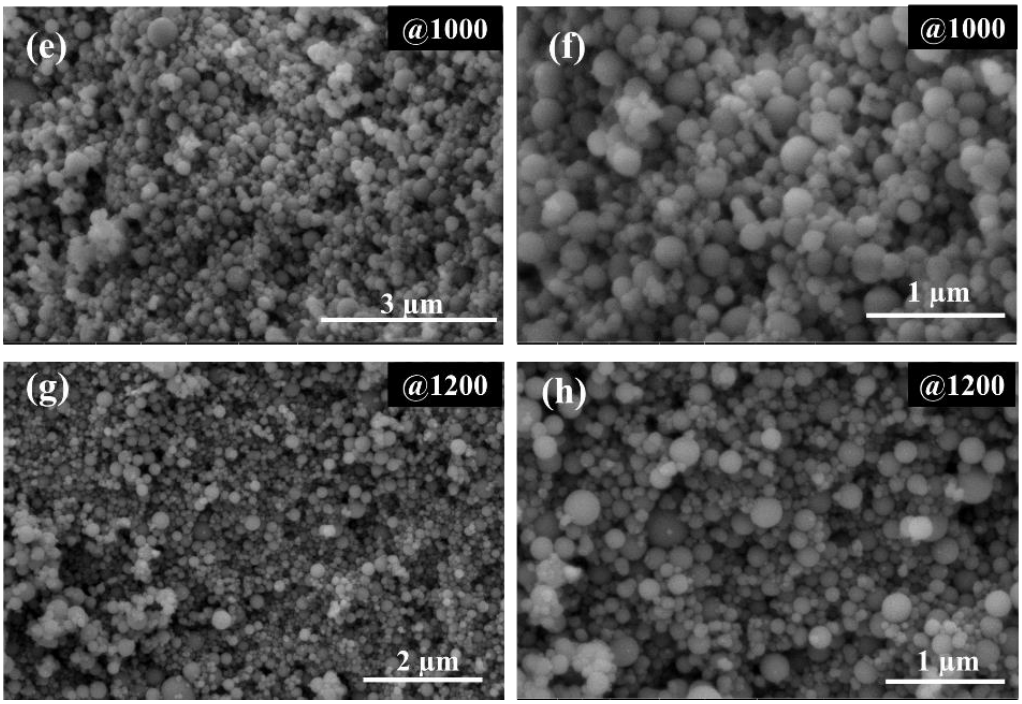

Figure 3. 13. The SEM images of the samples pyrolyzed at different temperatures; (a) general morphology of UM600, (b) higher magnification image of UM600, (c) general morphology of UM800, (d) higher magnification image of UM800, (e) general morphology UM1000, (f) higher magnification image of UM1000, and (g) general morphology of UM1200, (h) higher magnification image of UM1200.

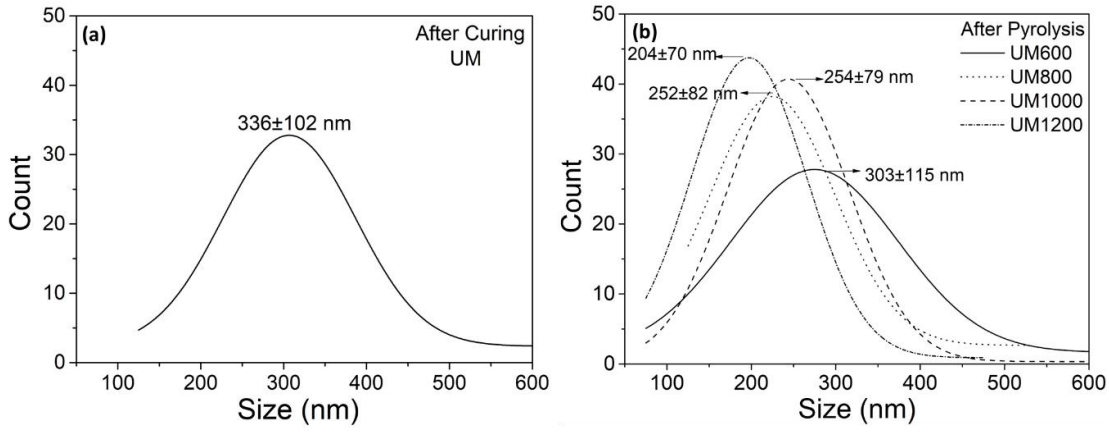

Figure 3. 14. The PSD plots of (a) cured sample at 140 ºC for 18h, and (b) pyrolyzed samples at 600-800-1000 and 1200 ºC for 2h under the Ar atmosphere.

While the size of cured polymeric spheres is 336±102 nm, after pyrolysis at 600,800,1000, and 1200 ˚C size of spheres are 303±115, 252±82 and 254±79 nm, 204±70 nm**,** respectively.

After pyrolysis process, ceramic yield, volumetric shrinkage and calculated SSA of samples were calculated by applying Formula (3.1 & 3.2), Formula (3.3), and Formula (3.4), respectively.

$$\text{Weight Loss (wt. \%)} = \frac{Mass\ (before\ pyrolysis) - Mass\ (after\ pyrolysis)}{Mass\ (before\ pyrolysis)} * 100 \quad (3.1)$$

$$\text{Ceramic Yield (wt. \%)} = 100 - \text{Weight Loss (wt. \%)} \quad (3.2)$$

$$\text{Volumetric Shrinkage (\%)} = \frac{Volume\ (before\ pyrolysis) - Volume\ (after\ pyrolysis)}{Volume\ (before\ pyrolysis)} * 100 \quad (3.3)$$

$$\text{Calculated SSA } (m^2/g) = \frac{4\pi r^2}{d_{SiOC}(\frac{4}{3})\pi(r^3)} \quad (3.4)$$

According to stirring types and pyrolysis temperatures, ceramic yield, volumetric shrinkage, calculated, and BET specific surface area of spheres are listed in Table 3.1.

When compared to samples by mixing with magnetic (MM1000) and ultrasonic probe sonicator (UM1000) pyrolyzed at 1000 ºC, the ceramic yield and volumetric shrinkage values of these samples are close to each other. Among the samples mixed with ultrasonic probe sonicator and pyrolyzed at different temperatures (600-800-1000-1200 ˚C), UM600 sample, obtaining by pyrolysis at 600 ˚C, has the highest (87.5 wt. %) ceramic yield and the lowest volumetric shrinkage (15.8%). The largest weight loss occurred in the process of organic to inorganic transition up to 800 ˚C.[106] UM1200 sample has the highest volumetric shrinkage (76.3%).

Calculated SSA values were obtained by using the radii obtained from the particle size measurements of the samples and by accepting the density of SiOC as 2.1 g/cm^3. Calculated SSA and BET SSA values of UM600 sample are different. By the calculated SSA, the bulk nonporous surface areas of the spheres can be determined.

Lower pyrolysis temperature (600 °C) causes transient micro and mesoporosity in the samples. Therefore, the calculated surface area and BET surface area measurement for this sample are different from each other.

Table 3. 1. The percentage of ceramic yields, volumetric shrinkage, calculated (SSA), and BET specific surface area of samples after pyrolysis.

Sample Code	Stirring Type	Pyrolysis Temperature (°C)	Ceramic Yield (wt.%)	Volumetric Shrinkage (%)	Calculated SSA (m^2/g)	SSA (m^2/g)
MM1000	Magnetic	1000	81.9	53.8	0.026	-
UM600	Sonicator	600	87.5	15.8	9.46	337.12
UM800	Sonicator	800	83.7	55.8	11.3	24.74
UM1000	Sonicator	1000	79.5	55.9	11.2	11.39
UM1200	Sonicator	1200	80.2	76.3	13.9	23.53

3.4. Structural Characterization of Spheres Derived from Silicone Resin

The FTIR spectra of cured and pyrolyzed samples are shown in Figure 3.15. In the spectra for cured sample, the adsorption of Si-CH_3 bond located around 774 cm^{-1} and 1274 cm^{-1}. With increasing pyrolysis temperatures, the intensity of the Si-CH_3 bonds decreased and disappeared. Samples have identical SiOC spectrum after pyrolysis at 800 °C, indicating that Si-C stretching peak centering 805 cm^{-1}, and also broad peak centering ~1050 cm^{-1}, corresponding Si-O stretching in Si-O-Si or Si-O-C.[66] Also, the broadband around 3500 cm^{-1} is referred to O-H stretching.[109]

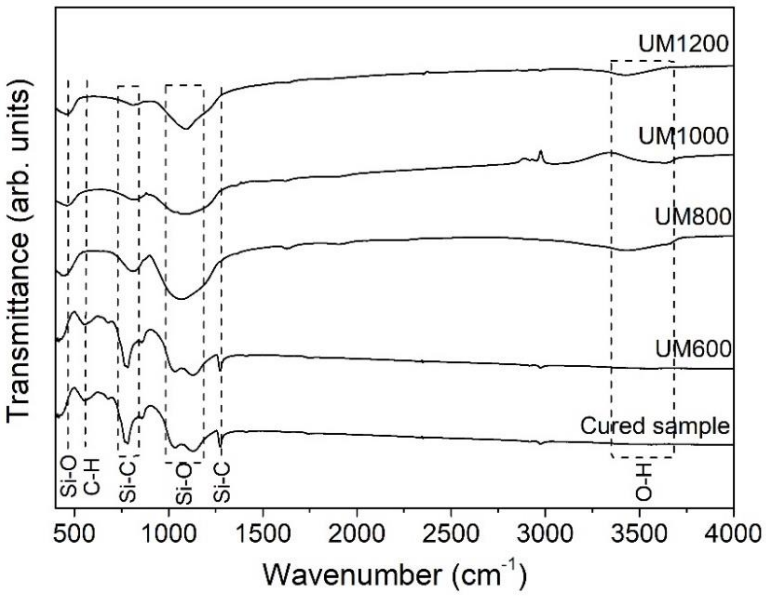

Figure 3. 15. The FTIR spectra of cured sample at 140 ^{o}C for 18 h, and pyrolyzed samples at different temperatures (600-800-1000 and 1200 ^{o}C) for 2h under Ar atmosphere.

TGA was applied to examine the thermal stability of samples under the oxygen atmosphere. As shown in Fig. 3.16, UM600 sample showed (12 %wt.) weight loss from 500 ^{o}C to 1000 ^{o}C. That might be explained by the fact that UM600 sample (obtained by pyrolysis at 600 ^{o}C) has a polymeric-ceramic structure. So the volatile components in the structure are removed at high temperatures and weight loss is experienced.

On the other hand, TGA oxidation experiments show that the pyrolyzed samples at various temperatures are strongly resistant to air oxidation up to 1000 ^{o}C. Maximum weight gain values are < 6, 4, and 2 wt% for UM800, UM1000 and UM1200 samples, respectively. With the rising of pyrolysis temperature, weight change temperature increased, and weigh change decreased.

XRD patterns of samples are shown in Figure 3.17. Broad peaks between 10° and 30° range (2θ) indicate the characteristics of amorphous SiOC materials.[66] Also, metallic tin (ICDD 01-089-2958) peaks were observed at 31^{o},32^{o,} 44 ^{o}, and 45 ^{o} due to the Tin catalyst.[110]

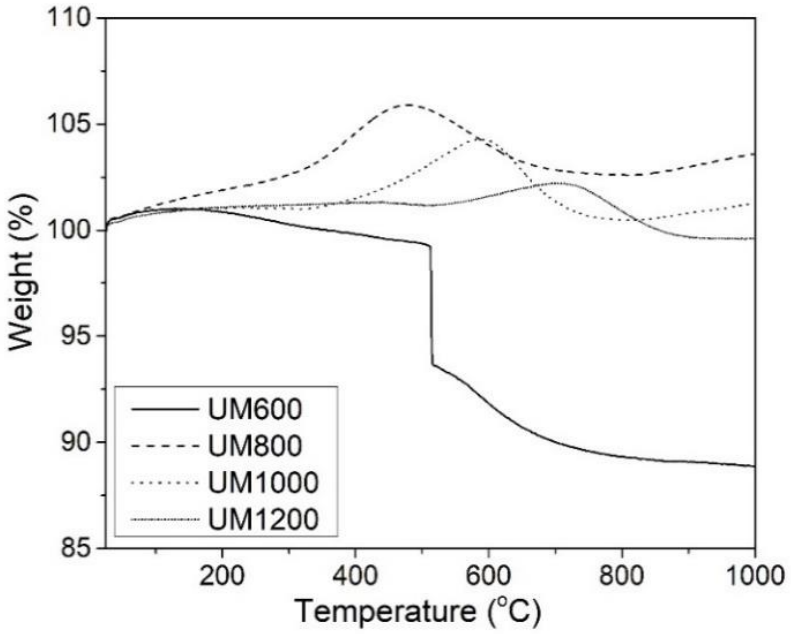

Figure 3. 16. The TGA results of samples obtained by pyrolysis at 600,800 1000 and 1200 ^{o}C for 2h under the oxygen atmosphere.

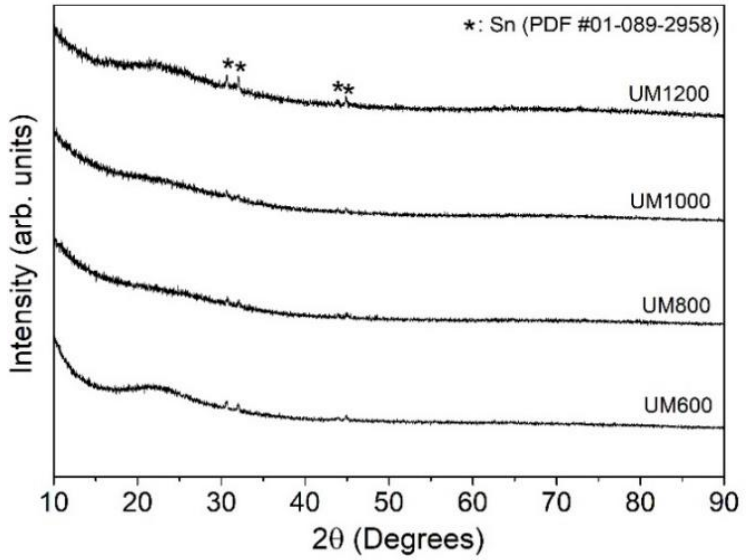

Figure 3. 17. XRD patterns of samples obtained by pyrolysis at 600,800 1000 and 1200 °C for 2h under the Ar atmosphere.

Since the spheres produced by the emulsion method using preceramic resin (MK powder) were smaller and had more homogeneous size distribution than those produced by using preceramic oil (PHMS), the experiments of coating SiOC substrates with TiO_2 were carried out with MK derived SiOC spheres for use in adsorption and photocatalytic experiments.

3.5. Morphological Characterization of TiO_2 Coated SiOC Spheres

Microstructural and elemental analysis of TiO_2 coated SiOC spheres was conducted to investigate whether TiO_2 was homogeneously coated into SiOC substrates.

SEM images and EDX elemental mappings of TiO_2 coated SiOC spheres produced by using SiOC substrate pyrolyzed at different temperatures (600, 800, 1000 and 1200 ^oC) and containing different (5-10 and 20 %) amounts of TiO_2 are shown in Figure 3.18, 3.19, 3.20 and 3.21. EDX elemental mapping analysis was conducted to show the distribution of silicon (Si), oxygen (O), carbon (C), and titanium (Ti) elements in the samples.

SEM images show that the spherical structures of the samples were not deteriorated after coating with titanium dioxide.

As it can be seen from the EDX mapping analysis results of samples, containing different amounts of TiO_2, for each pyrolysis temperatures, titanium homogeneously dispersed. And also, the increasing amount of titanium dioxide was supported by increasing titanium (%wt.) in the EDX results.

Besides, the atomic percentages of titanium in samples are given in Table 3.2. Since the specific and small part of the sample was examined by EDX analysis, the results were presented only to show that the amount of titanium increases with the increase of the coating amount.

For UM600T5, UM800T5, UM1000T5, and UM1200T5 samples, at the lowest titanium dioxide coating amount (5%), atomic percentages of titanium in the samples are 0.34, 0.92, 0.42 and 0.55, respectively.

By increasing the coating amount to 20%, for UM600T20, UM800T20, UM1000T20, and UM1200T20 samples, atomic percentages of titanium in the samples are 1.62, 2.30, 0.78, and 2.26, respectively.

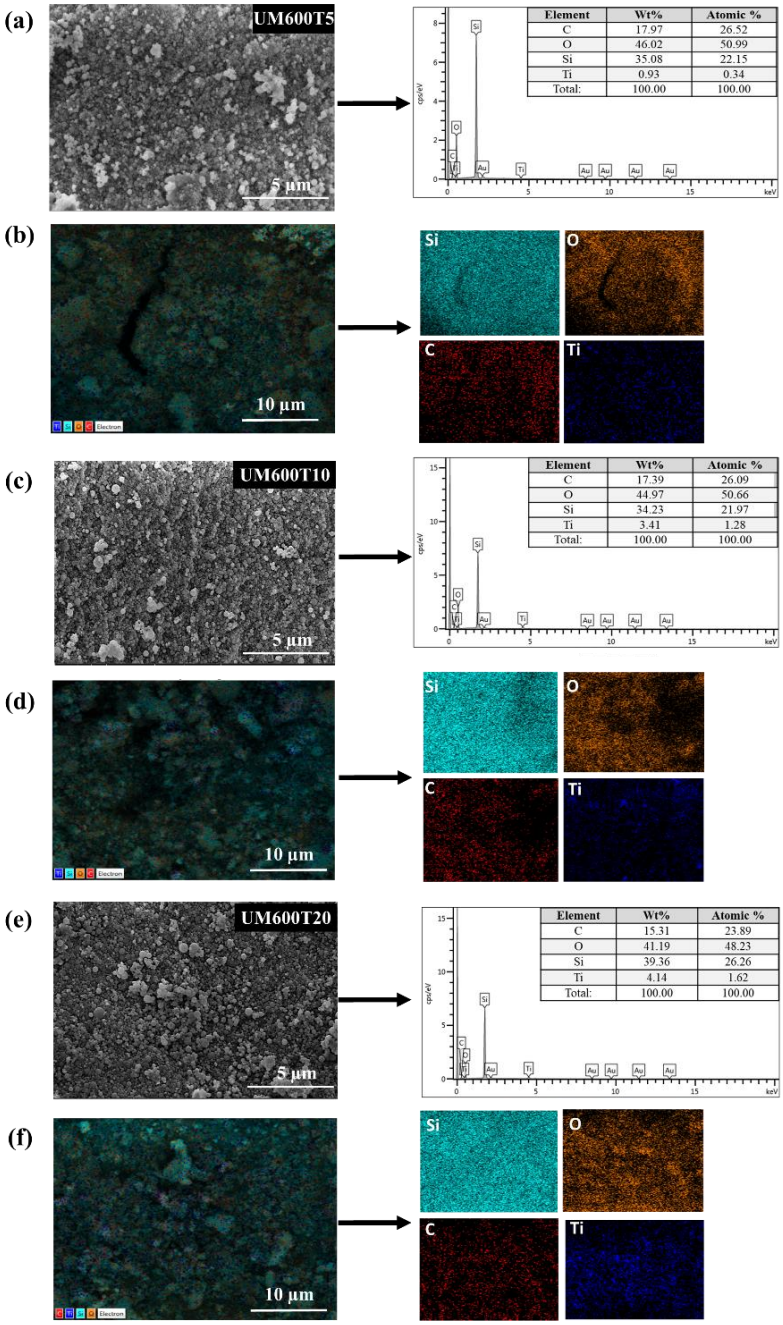

Figure 3. 18. SEM images and EDX elemental mappings of SiOC+TiO_2 samples produced by using SiOC substrate pyrolyzed at 600 ^oC and containing TiO_2; (a) SEM image and EDX spectroscopy of UM600T5 containing 5% TiO_2, (b) EDX mapping analysis of UM600T5, (c) SEM image and EDX spectroscopy of UM600T10 containing 10% TiO_2, (d) EDX mapping analysis of UM600T10, (e) SEM image and EDX spectroscopy of UM600T20 containing 20% TiO_2, and (f) EDX mapping analysis of UM600T20.

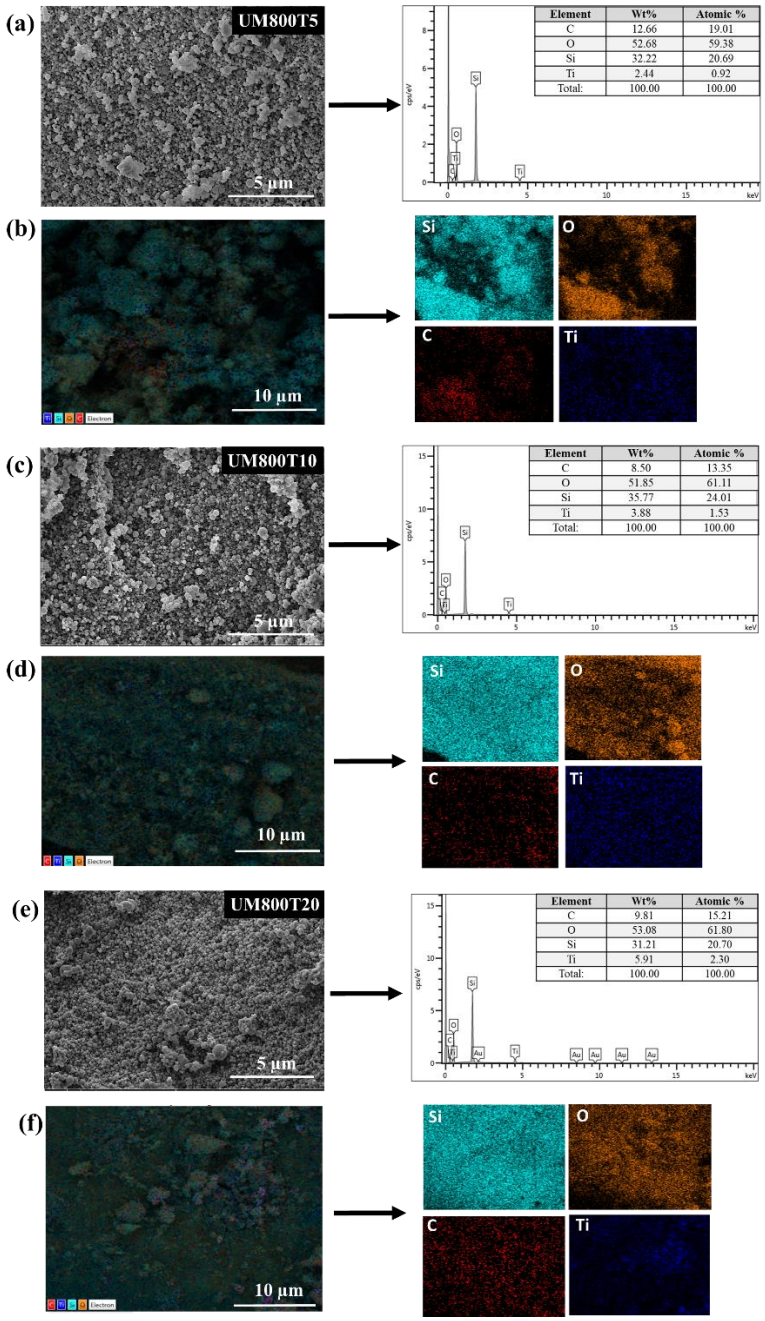

Figure 3. 19. SEM images and EDX elemental mappings of SiOC+TiO_2 samples produced by using SiOC substrate pyrolyzed at 800 ºC and containing TiO_2; (a) SEM image and EDX spectroscopy of UM800T5 containing 5% TiO_2, (b) EDX mapping analysis of UM800T5, (c) SEM image and EDX spectroscopy of UM800T10 containing 10% TiO_2, (d) EDX mapping analysis of UM800T10, (e) SEM image and EDX spectroscopy of UM800T20 containing 20% TiO_2, and (f) EDX mapping analysis of UM800T20.

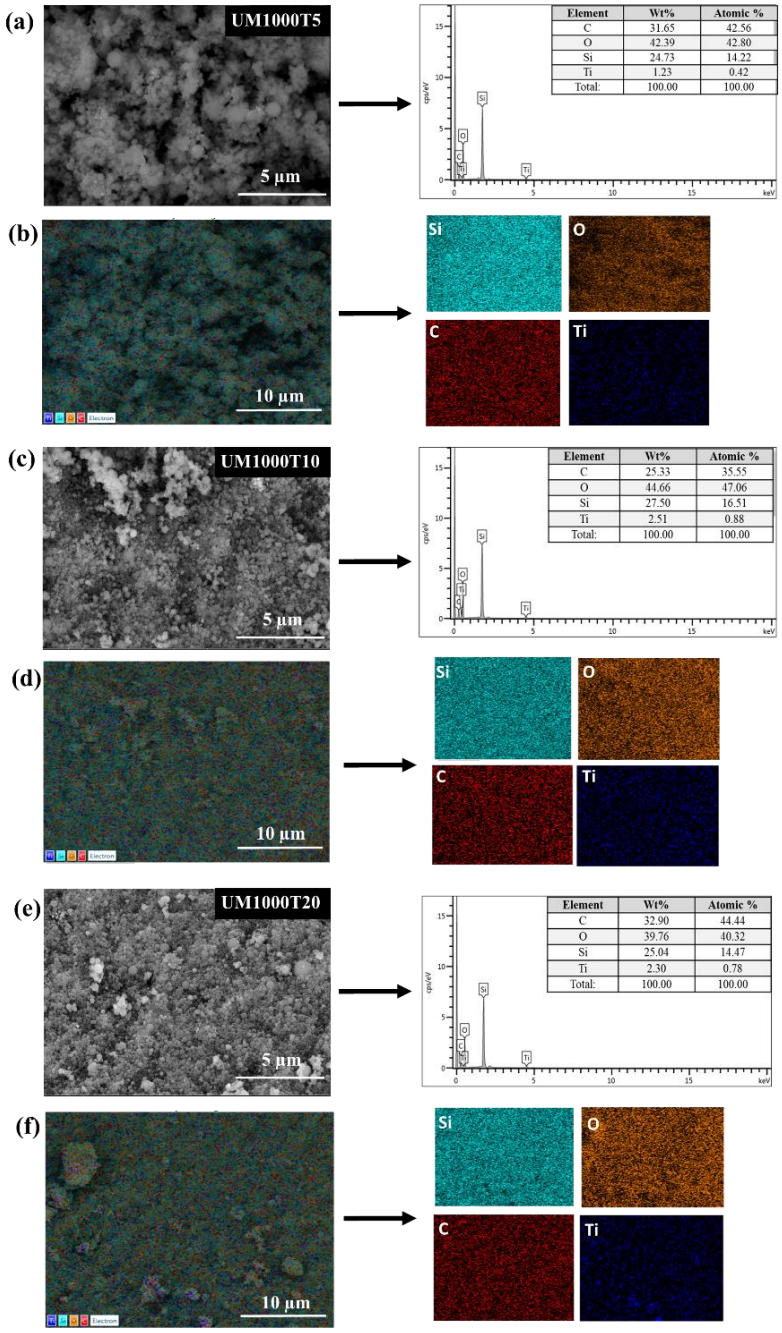

Figure 3. 20. SEM images and EDX elemental mappings of SiOC+TiO_2 samples produced by using SiOC substrate pyrolyzed at 1000 ^oC and containing TiO_2; (a) SEM image and EDX spectroscopy of UM1000T5 containing 5% TiO_2, (b) EDX mapping analysis of UM1000T5, (c) SEM image and EDX spectroscopy of UM1000T10 containing 10% TiO_2, (d) EDX mapping analysis of UM1000T10, (e) SEM image and EDX spectroscopy of UM1000T20 containing 20% TiO_2, and (f) EDX mapping analysis of UM1000T20.

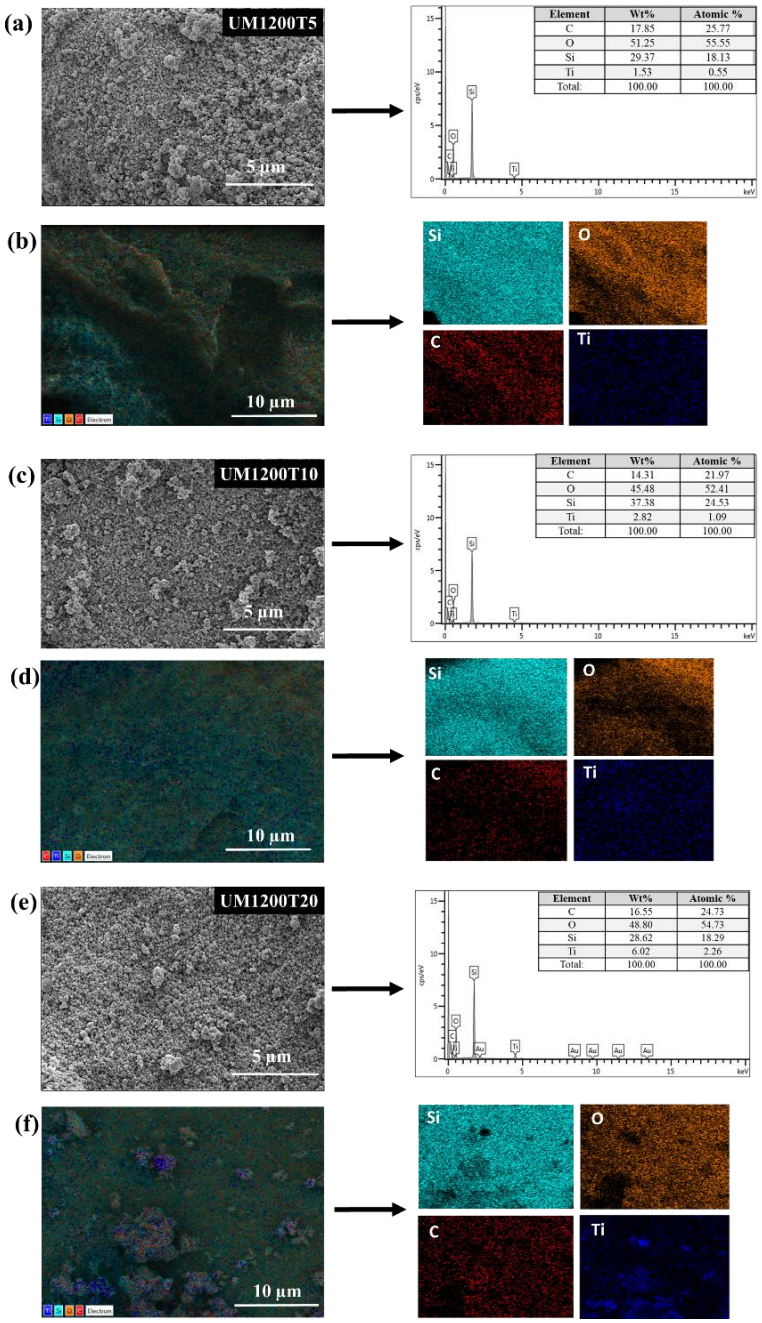

Figure 3. 21. SEM images and EDX elemental mappings of SiOC+TiO_2 samples produced by using SiOC substrate pyrolyzed at 1200 ^oC and containing TiO_2; (a) SEM image and EDX spectroscopy of UM1200T5 containing 5% TiO_2, (b) EDX mapping analysis of UM1200T5, (c) SEM image and EDX spectroscopy of UM1200T10 containing 10% TiO_2, (d) EDX mapping analysis of UM1200T10, (e) SEM image and EDX spectroscopy of UM1200T20 containing 20% TiO_2, and (f) EDX mapping analysis of UM1200T20.

Table 3. 2. Titanium atomic percentages in samples obtained from EDX analysis.

Sample	Titanium Atomic (%)
UM600T5	0.34
UM600T10	1.28
UM600T20	1.62
UM800T5	0.92
UM800T10	1.53
UM800T20	2.3
UM1000T5	0.42
UM1000T10	0.88
UM1000T20	0.78
UM1200T5	0.55
UM1200T10	1.09
UM1200T20	2.26

3.6. Structural Characterization of TiO_2 Coated SiOC Spheres

a) Fourier Transform Infrared Spectra (FTIR) Analysis

FTIR spectra were taken from TiO_2 coated SiOC samples and shown in Figure 3.22. The bands of the Ti-O-Ti and Si-O-Ti bonds at 430 and 960 cm^{-1} [111, 112] did not appear in the FTIR spectra of the TiO_2 coated SiOC samples by the reason of the overlapping the bands of silica at the same wavenumbers.

Pure SiOC and TiO_2 coated SiOC samples have the same identical SiOC spectrum, indicating that Si-C stretching peak centering 805 cm^{-1}, and also broad peak centering ~1050 cm^{-1}, corresponding Si-O stretching in Si-O-Si or Si-O-C.[66] Also, the broadband around 3500 cm^{-1} is referred to as O-H stretching.[109]

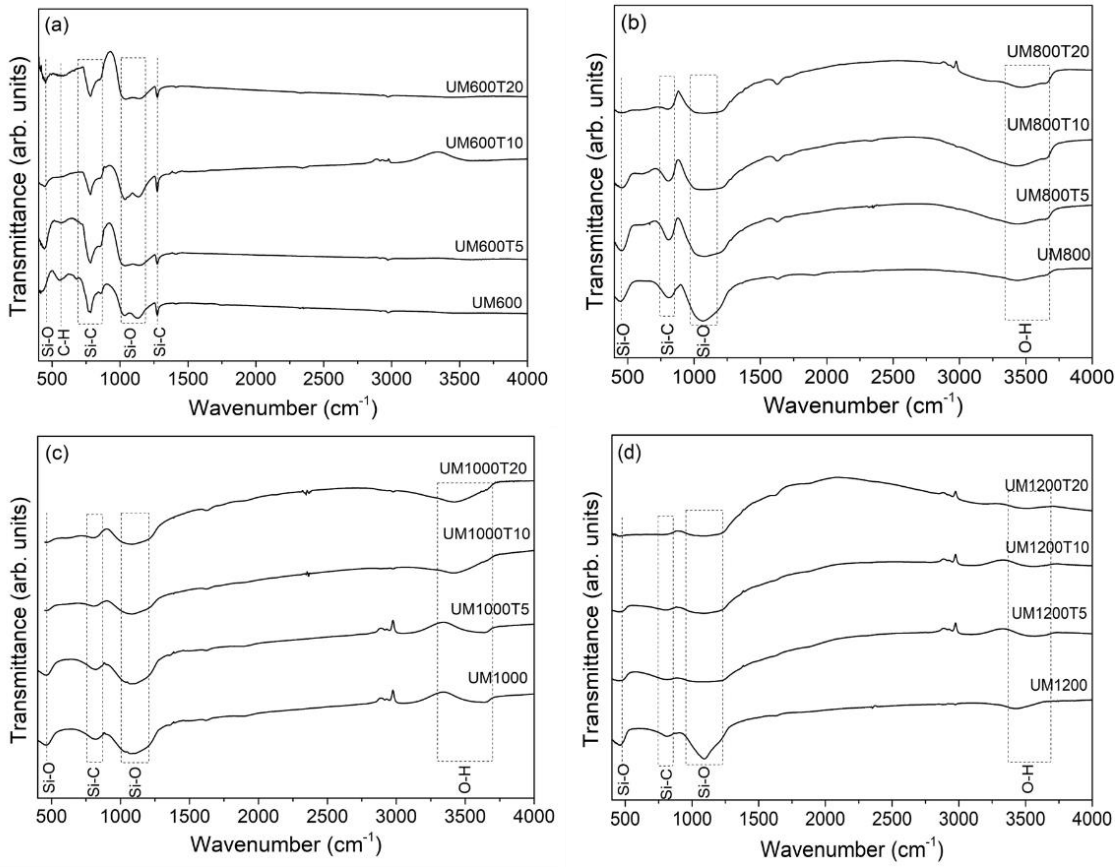

Figure 3. 22. FTIR analysis of TiO_2 coated SiOC samples produced by using SiOC substrate pyrolyzed (a) at 600 ^oC and containing different amounts of TiO_2, (b) at 800 ^oC and containing different amounts of TiO_2, (c) at 1000 ^oC and containing different amounts of TiO_2 and (d) at 1200 ^oC and containing different amounts of TiO_2.

b) X-Ray Diffraction (XRD) Analysis

XRD patterns of TiO_2 coated SiOC samples are shown in Figure 3.23. With the increase in the amount of TiO_2, the titanium dioxide (Anatase) peaks (at 25^o, 37^o, 48 ^{o}, 54 ^{o}, 55 ^{o}, and 63 ^{o}) are clearer and intense. After the samples were coated with titanium dioxide, the peaks of the metallic tin (at 31^o and 32^o) disappeared in the XRD pattern.

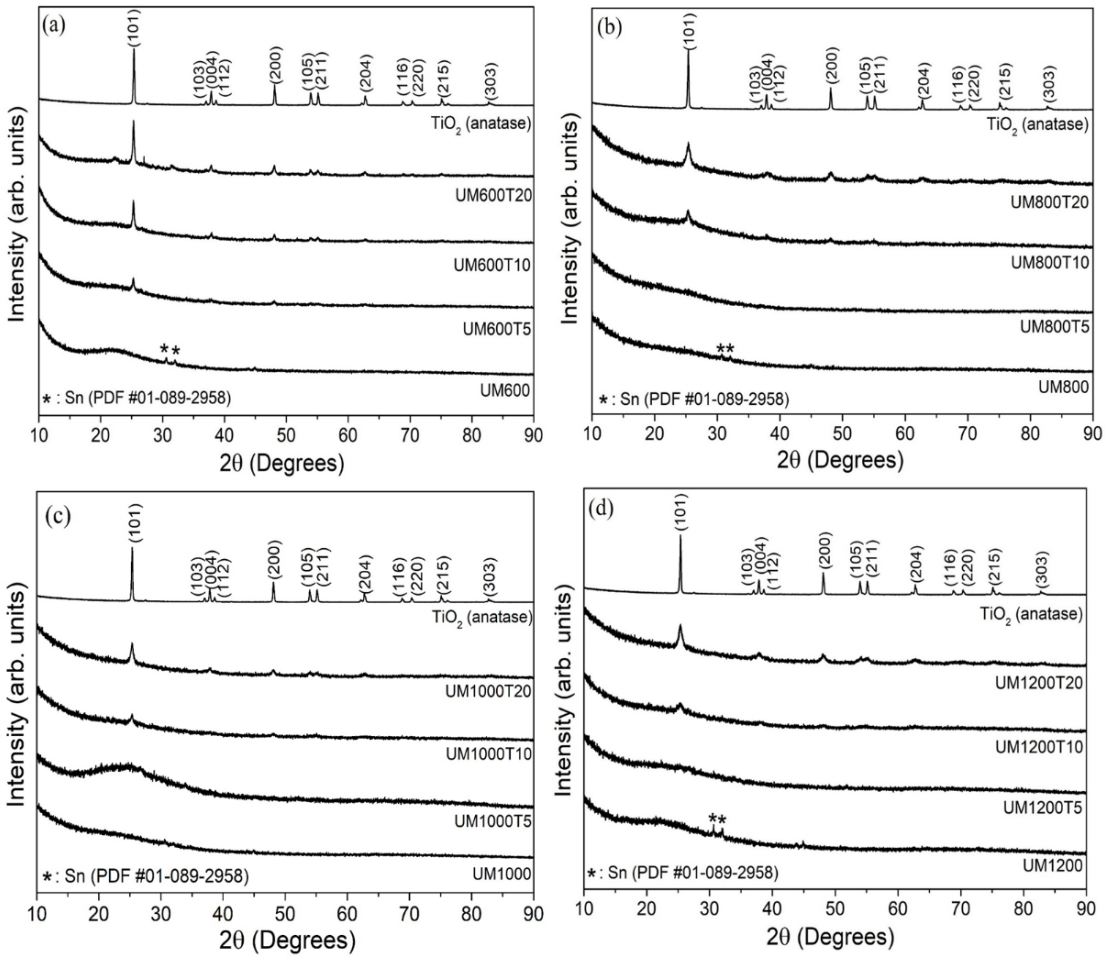

Figure 3. 23. XRD patterns of TiO_2 coated SiOC samples produced by using SiOC substrate pyrolyzed (a) at 600 ^oC and containing TiO_2, (b) at 800 ^oC and containing TiO_2, (c) at 1000 ^oC and containing TiO_2 and (d) at 1200 ^oC and containing TiO_2.

c) Nitrogen Adsorption-Desorption Analysis

Nitrogen (N_2) adsorption-desorption analysis was carried out to determine the BET SSA and pore structure of the pure SiOC samples and TiO_2 coated SiOC samples. The samples were firstly degassed at 200 ^oC for 12 h before analysis. Specific surface area (SSA) was determined from a BET (Brunauer–Emmett–Teller) analysis. Also, pore size distributions were obtained from the desorption part of the isotherms.

Table 3.3. shows nitrogen (N_2) adsorption-desorption analysis results of selected samples.

Table 3. 3. N_2 ads/des. results of SiOC and SiOC+TiO_2 samples.

Sample	BET (m^2/g)	BJH Desorption Cumulative volume of pores (cm^3/g)	BJH Desorption average pore width (4V/nm)
UM600	337	0.09	9.2
UM600T5	346	0.27	15.6
UM600T20	296	0.23	17.5
UM800	24.7	0.21	15.2
UM800T5	30.4	-	-
UM800T20	31.9	0.19	17.9
UM1000	11.4	0.07	20.1
UM1000T5	24.6	-	-
UM1000T20	41.4	0.19	15.9
UM1200	23.5	0.16	19.6
UM1200T5	27.6	-	-
UM1200T20	35.9	0.15	13.6

UM600 sample has the highest surface area with 337 m^2/g among pure SiOC samples. With the increase of pyrolysis temperature, micro and mesopores decreased and the surface areas of the samples (UM800, UM1000, and UM1200) decreased to 24.7, 11.4 and 23.5 m^2/g, respectively.

By covering the SiOC substrate (UM600) with the highest calculated amount (20%) of titanium dioxide, the surface area has decreased to 296 m^2/g. This may be due to the covering of some micropores on the surface with titanium dioxide.

On the other hand, for other sample sets (pyrolyzed at 800,1000 and 1200 ^{o}C), the surface area increased with the increase in the amount of titanium dioxide.

3.7. Adsorption-Photocatalytic Performance Measurements of TiO_2 Coated SiOC Spheres on MB Dye

Adsorption and photocatalytic performances of pure SiOC and various amount of TiO_2 coated SiOC spheres were examined by the decrease in the concentration of MB dye solution.

Initially, MB stock solution (0.03 mM=10 ppm) was prepared by adding MB powder into DI water.

Adsorption experiments for pure SiOC samples were conducted in the dark for 2, 6, and 24 h. 15 mg of SiOC samples were dispersed in 30 mL of the prepared MB solution. This solution was mixed with a magnetic stirrer at 500 rpm in the dark. After 2 h, 6 h and 24 h 2 ml of sample were taken from the solution with a micropipette.

For the photocatalytic experiments, initially, 15 mg of various amounts (0-5-10 and 20%) TiO_2 coated SiOC samples were dispersed in 30 mL of the prepared MB solution. This solution was mixed with a magnetic stirrer at 500 rpm for 2h in the dark to achieve adsorption-desorption equilibrium between powders and MB dye. After 2 h of mixing in the dark, 2 ml of sample was taken from the solution with a micropipette. Then the solution was placed 20 cm across to UV light source and stirred at 500 rpm for 2h in a UV lamp cabin system having a 300 Watt UV light source (Osram, UltraVitalux). During mixing under a UV light source, at time intervals (15, 30, 45, 60, 90, and 120) 2 ml of samples were taken from the solution with a micropipette. Ultraviolet-visible (UV-Vis) spectrophotometer (UV2550, SHIMADZU) was used to measure changes at major absorbance peak (664 nm) of MB solutions. According to Lambert-Beer law[113], concentration and absorbance of the solution have a proportional relationship. Therefore, the concentration of solutions for different (0-15-30-45-60-90 and 120 min.) durations of UV irradiations was calculated by using the absorbance value of initially prepared MB solution with known molarity.

Figure 3.24 shows the adsorption percentage of the pure SiOC (UM600, UM800, UM1000, and UM1200) samples at different contact times. As it can be seen from Fig. 3.25, at the end of the 24 h, UM600, UM800, UM1000 and UM1200 samples have 2%,

18%, 36% and 64% adsorption percentages, respectively. In adsorption experiments to remove MB dye from water, as the pyrolysis temperatures increases, samples exhibited much higher adsorption results.

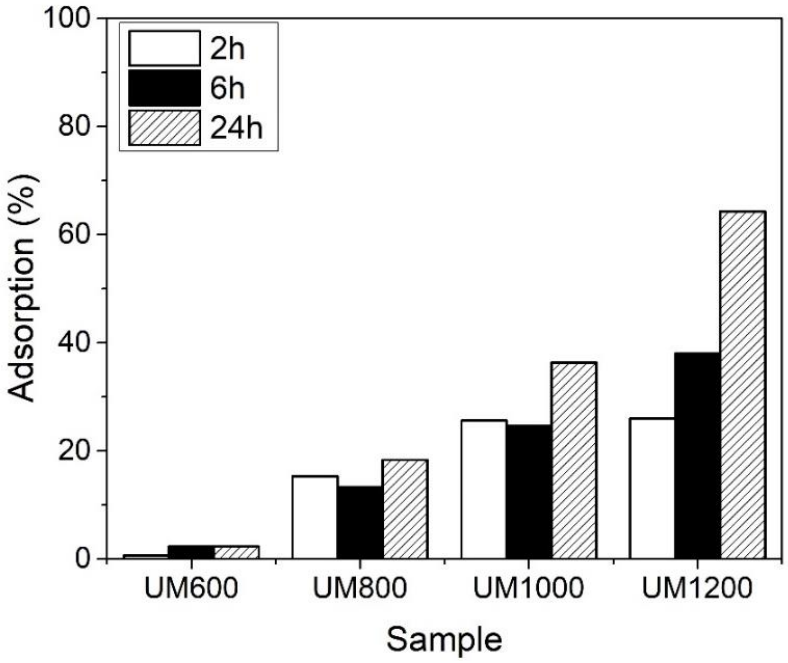

Figure 3. 24. Adsorption percentages of the MB dye onto UM600, UM800, UM1000, and UM1200 samples at 2-24 h contact times.

Photocatalytic performance results of the pure SiOC substrate, produced by pyrolysis at 600 ºC, and TiO_2 coated SiOC samples are shown in Figure 3.25. The change in the initial MB concentration (C_0 = 0.03 mM) by reaction with the UM600, UM600T5, UM600T10, and UM600T20 samples as a result of adsorption time (2h) in the dark and photodegradation time (2h) under UV irradiation is shown in Figure 3.25(a). Figure 3.25(b) shows photocatalytic degradation kinetics of samples.

The calculated photodegradation rate constants are shown in Table 3.4. While the pure SiOC (UM600) sample has the 0.57 $x10^{-3}$ min^{-1} rate constant, the UM60020 sample has the highest rate constant with the $23x10^{-3}$ min^{-1}.

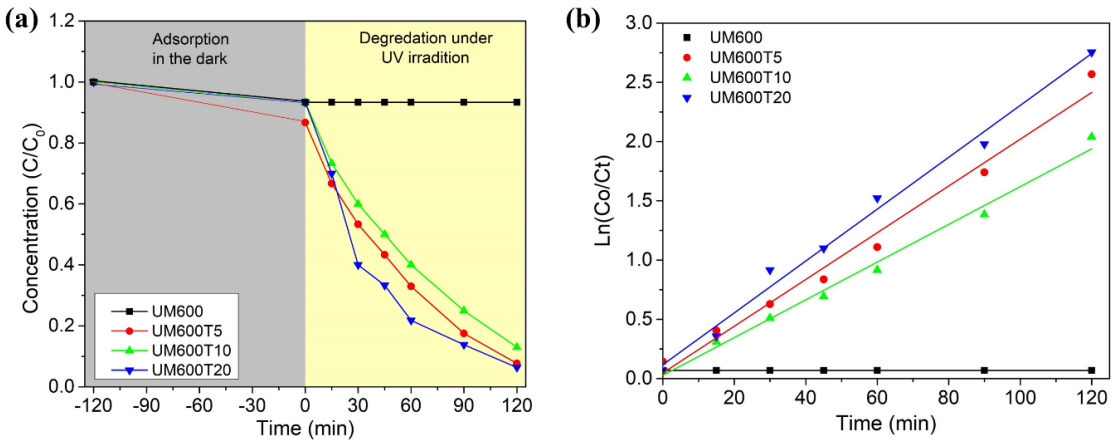

Figure 3. 25. (a) Degradation ratio of MB (C_o:0.03 mM) solution by the reaction with pure SiOC substrate produced by pyrolysis at 600 ^oC and samples containing 5%, 10%, and 20% amount of TiO_2, and (b) kinetic curves of the MB degradation.

Table 3. 4. Photodegradation rate constants of pure SiOC (UM600) sample and various amount of (5%, 10%, and 20%) TiO_2 coated SiOC (UM600T5, UM600T10, and UM600T20) samples. (k (min^{-1})

Sample	**Rate Constant (k; 10^{-3} x min^{-1})**
UM600	0.57
UM600T5	21
UM60010	17
UM60020	23

Photocatalytic performance results of the pure SiOC substrate, produced by pyrolysis at 800 ^oC, and TiO_2 coated SiOC samples are shown in Figure 3.26. The change in the initial MB concentration (C_0 = 0.03 mM) by reaction with the UM800, UM800T5, UM800T10, and UM800T20 samples as a result of adsorption time (2h) in the dark and photodegradation time (2h) under UV irradiation is shown in Figure 3.26(a). Figure 3.26(b) shows photocatalytic degradation kinetics of samples.

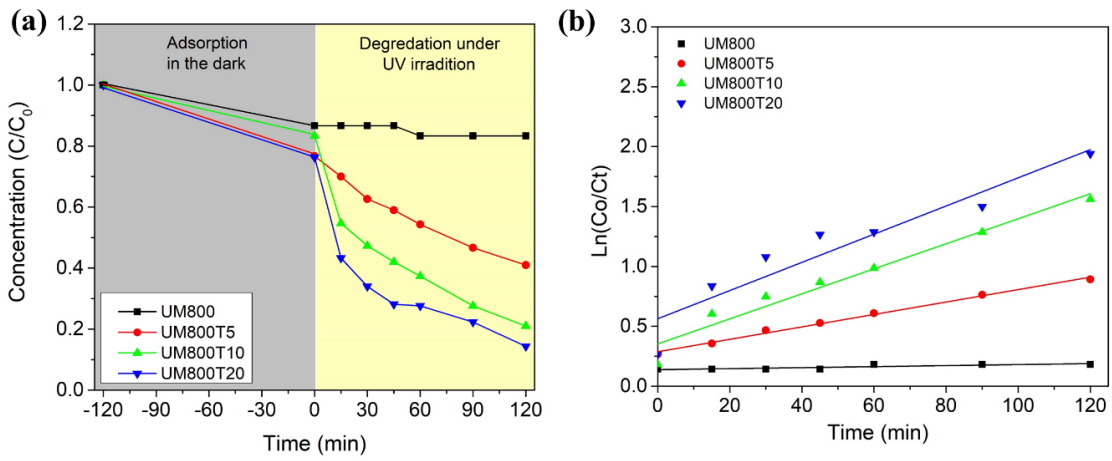

Figure 3. 26. (a) Degradation ratio of MB (C_o:0.03 mM) solution by the reaction with pure SiOC substrate produced by pyrolysis at 800 ^oC and samples containing 5%, 10%, and 20% amount of TiO_2, and (b) kinetic curves of the MB degradation.

The calculated photodegradation rate constants are shown in Table 3.5. While the pure SİOC (UM800) sample has the 1.5 $x10^{-3}$ min^{-1} rate constant, the UM80020 sample has the highest rate constant with the $16x10^{-3}$ min^{-1}.

Table 3. 5. Photodegradation rate constants of pure SiOC (UM800) sample and various amount of (5%, 10%, and 20%) TiO_2 coated SiOC (UM800T5, UM800T10, and UM800T20) samples. (k (min^{-1})

Sample	Rate Constant (k; 10^{-3} x min^{-1})
UM800	1.5
UM800T5	7.4
UM80010	13
UM80020	16

Photocatalytic performance results of the pure SiOC substrate, produced by pyrolysis at 1000 ºC, and TiO_2 coated SiOC samples are shown in Figure 3.27. The change in the initial MB concentration (C_0 = 0.03 mM) by reaction with theUM1000, UM1000T5, UM1000T10, and UM1000T20 samples as a result of adsorption time (2h) in the dark and photodegradation time (2h) under UV irradiation is shown in Figure 3.27(a). Figure 3.27(b) shows photocatalytic degradation kinetics of samples.

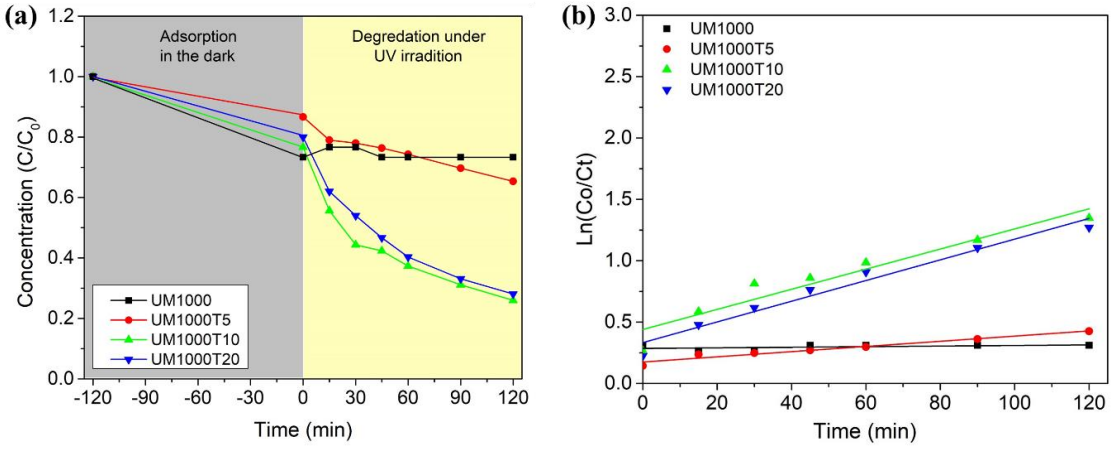

Figure 3. 27. (a) Degradation ratio of MB (C_o:0.03 mM) solution by the reaction with pure SiOC substrate produced by pyrolysis at 1000 ºC and samples containing 5%, 10%, and 20% amount of TiO_2, and (b) kinetic curves of the MB degradation.

The calculated photodegradation rate constants are shown in Table 3.6. While the pure SiOC (UM1000) sample has the 2.5 $x10^{-3}$ min^{-1} rate constant, UM100010 sample has the highest rate constant with the $11x10^{-3}$ min^{-1}.

Photocatalytic performance results of the pure SiOC substrate, produced by pyrolysis at 1200 ºC, and TiO_2 coated SiOC samples are shown in Figure 3.28. The change in the initial MB concentration (C_0 = 0.03 mM) by reaction with the UM1200, UM1200T5, UM1200T10, and UM1200T20 samples as a result of adsorption time (2h) in the dark and photodegradation time (2h) under UV irradiation is shown in Figure 3.28(a). Figure 3.28(b) shows photocatalytic degradation kinetics of samples.

Table 3. 6. Photodegradation rate constants of pure SiOC (UM1000) sample and various amount of (5%, 10%, and 20%) TiO_2 coated SiOC (UM1000T5, UM1000T10, and UM1000T20) samples. (k (min^{-1})

Sample	Rate Constant (k; 10^{-3} x min^{-1})
UM1000	2.5
UM1000T5	3.5
UM100010	11
UM100020	10

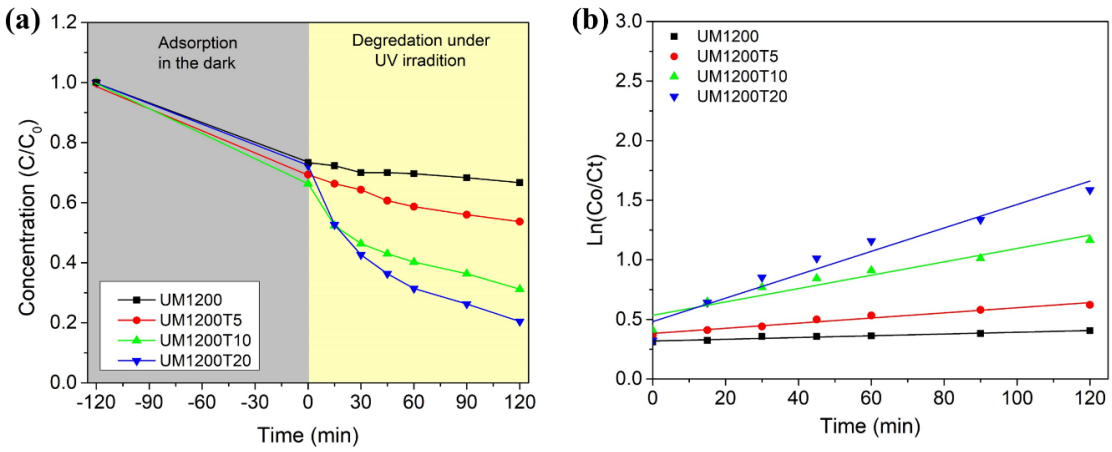

Figure 3. 28. (a) Degradation ratio of MB (C_o:0.03 mM) solution by the reaction with pure SiOC substrate produced by pyrolysis at 1200 ^oC and samples containing 5%, 10%, and 20% amount of TiO_2, and (b) kinetic curves of the MB degradation.

The calculated photodegradation rate constants are shown in Table 3.7. While the pure SiOC (UM1200) sample has the 3.3 $x10^{-3}$ min^{-1} rate constant, UM120020 sample has the highest rate constant with the $13x10^{-3}$ min^{-1}.

Table 3. 7. Photodegradation rate constants of pure SiOC (UM1200) sample and various amount of (5%, 10%, and 20%) TiO_2 coated SiOC (UM1200T5, UM1200T10, and UM1200T20) samples. (k (min^{-1})

Sample	Rate Constant (k; 10^{-3} x min^{-1})
UM1200	3.3
UM1200T5	5.2
UM120010	9.6
UM120020	13

Photo-degradation efficiencies of pure SiOC and TiO_2 coated SiOC samples are given in Figure 3.29. While the photo-degradation percentages of the samples were calculated, the percentages of adsorption performed before the UV test were subtracted from the entire results. In summary, under UV irradiation, while pure SiOC (UM1000) sample showed the lowest (1%) photo-degradation efficiency, samples coated with titanium dioxide (UM600T20) showed 87% photo-degradation efficiency. It was observed that photo-degradation efficiency increases with the increase in the amount of titanium dioxide in all sample sets.

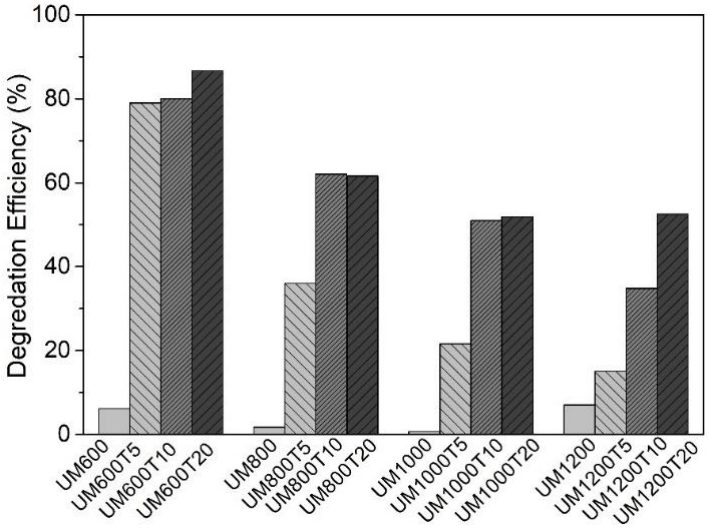

Figure 3. 29. Photodegradation Efficiency (%) of all samples.

At the end of the photocatalytic experiments for all samples, the decolorization of MB dye aqueous solution is illustrated in Figure 3.30.

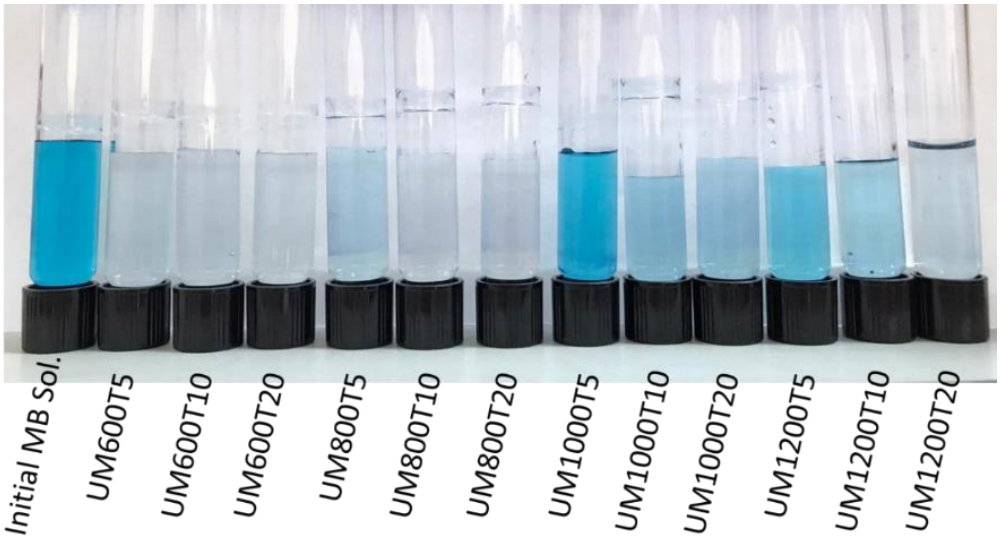

Figure 3. 30. The decolorization of MB solution after photocatalytic experiments.

CHAPTER 4

CONCLUSIONS

Porous silicon oxycarbide (SiOC) submicron spheres were produced via the emulsion method by using economic and commercial preceramic polymers. After obtaining homogeneously distributed submicron polymeric spheres, curing was conducted this was followed by the pyrolysis at different temperatures (600-800-1000 and 1200 ° C). Upon pyrolysis at 600-800-1000 and 1200 ° C, the size of the SiOC submicron spheres were measured as 303±115, 252±82, 254±79 and 204±70, respectively. All samples were coated with titanium dioxide precursor ((Titanium(IV) n-butoxide) in order to produce titania coated SiOC spheres. For this aim, samples were heat-treated at 450 °C/air to obtain the photocatalytically active anatase (titanium dioxide) coated SiOC ceramic composites.

With the increase in the amount of TiO_2 in samples, the *anatase related* peaks were started to be clearer in the resulted XRD patterns of SiOC+TiO_2 samples (corroborated also be SEM-EDX). BET specific surface area (SSA) and pore structures of the pure SiOC and TiO_2 coated SiOC samples were characterized by nitrogen adsorption-desorption analysis. UM600 sample, pyrolyzed at 600 °C, has the highest surface area with 337 m^2/g and microporosity among other SiOC samples. With the increase of the pyrolysis temperature, micropores disappeared, the surface areas of the samples (UM1000, and UM1200) started to decrease to 11.4, and 23.5 m^2/g, respectively.

Water purification experiments were carried out both by adsorption and photocatalytic degradation using methylene blue dye. Adsorption experiments (in the dark) were performed only for SiOC samples produced at different pyrolysis temperatures. UM1200 sample showed the best adsorption efficiency with 64% at the end of 24h. Photocatalytic experiments (under UV irradiation) were performed for both as SiOC and titania coated SiOC samples. UM600T20 sample, obtained by coating SiOC substrate (pyrolyzed at 600 °C) with 20% wt. titania showed the best photodegradation efficiency reaching 87%. Total removal efficiency (adsorption, followed by photodegradation) of the sample UM600T20 was found to be 94%.

REFERENCES

1. Kumar, M.; Puri, A., A review of permissible limits of drinking water. *Indian journal of occupational and environmental medicine* 2012, *16* (1), 40.
2. Liu, J.; Dorjderem, A.; Fu, J.; Lei, X.; Macer, D., Water Ethics and Water Resource Management. 2011.
3. Inyinbor Adejumoke, A.; Adebesin Babatunde, O.; Abimbola, O.; Adelani-Akande Tabitha, A., Water pollution: effects, prevention, and climatic impact. *Water Challenges of an Urbanizing World* 2018, 33.
4. Gürses, A.; Doğar, Ç.; Yalçın, M.; Açıkyıldız, M.; Bayrak, R.; Karaca, S., The adsorption kinetics of the cationic dye, methylene blue, onto clay. *Journal of Hazardous Materials* 2006, *131* (1-3), 217-228.
5. Haseena, M.; Malik, M. F.; Javed, A.; Arshad, S.; Asif, N.; Zulfiqar, S.; Hanif, J., Water pollution and human health. *Environmental Risk Assessment and Remediation* 2017, *1* (3), 16-19.
6. Gnanasekaran, L.; Hemamalini, R.; Rajendran, S.; Qin, J.; Yola, M. L.; Atar, N.; Gracia, F., Nanosized Fe3O4 incorporated on a TiO2 surface for the enhanced photocatalytic degradation of organic pollutants. *Journal of Molecular Liquids* 2019, *287*, 110967.
7. Wu, Z.; Huang, W.; Shan, X.; Li, Z., Preparation of a porous graphene oxide/alkali lignin aerogel composite and its adsorption properties for methylene blue. *International Journal of Biological Macromolecules* 2020, *143*, 325-333.
8. Li, J.; Zheng, L.; Liu, H., A novel carbon aerogel prepared for adsorption of copper (II) ion in water. *Journal of Porous Materials* 2017, *24* (6), 1575-1580.
9. Liou, T.-H.; Lin, M.-H., Characterization of graphene oxide supported porous silica for effectively enhancing adsorption of dyes. *Separation Science and Technology* 2020, *55* (3), 431-443.

10. Pan, J.; Ren, J.; Xie, Y.; Wei, X.; Guan, Y.; Yan, X.; Tang, H.; Cheng, X., Porous SiOC composites fabricated from preceramic polymers and wood powders for efficient dye adsorption and removal. *Research on Chemical Intermediates* 2017, *43* (7), 3813-3832.

11. Akpan, U. G.; Hameed, B. H., Parameters affecting the photocatalytic degradation of dyes using TiO2-based photocatalysts: a review. *Journal of hazardous materials* 2009, *170* (2-3), 520-529.

12. Vilar, V. J.; Botelho, C. M.; Boaventura, R. A., Methylene blue adsorption by algal biomass based materials: biosorbents characterization and process behaviour. *Journal of hazardous materials* 2007, *147* (1-2), 120-132.

13. Huang, C.-H.; Chang, K.-P.; Ou, H.-D.; Chiang, Y.-C.; Wang, C.-F., Adsorption of cationic dyes onto mesoporous silica. *Microporous and Mesoporous Materials* 2011, *141* (1-3), 102-109.

14. Hameed, B.; Ahmad, A.; Latiff, K., Adsorption of basic dye (methylene blue) onto activated carbon prepared from rattan sawdust. *Dyes and pigments* 2007, *75* (1), 143-149.

15. Gupta, V., Application of low-cost adsorbents for dye removal–a review. *Journal of environmental management* 2009, *90* (8), 2313-2342.

16. Salleh, M. A. M.; Mahmoud, D. K.; Karim, W. A. W. A.; Idris, A., Cationic and anionic dye adsorption by agricultural solid wastes: A comprehensive review. *Desalination* 2011, *280* (1-3), 1-13.

17. Chemicalize. https://chemicalize.com/ (Accessed:19.05.2020).

18. Zhang, W.; Zhang, L.; Zhao, H.; Li, B.; Ma, H., A two-dimensional cationic covalent organic framework membrane for selective molecular sieving. *Journal of Materials Chemistry A* 2018, *6* (27), 13331-13339.

19. Auta, M.; Hameed, B., Chitosan–clay composite as highly effective and low-cost adsorbent for batch and fixed-bed adsorption of methylene blue. *Chemical Engineering Journal* 2014, *237*, 352-361.

20. Eren, E.; Afsin, B., Investigation of a basic dye adsorption from aqueous solution onto raw and pre-treated bentonite surfaces. *Dyes and Pigments* 2008, *76* (1), 220-225.

21. Patel, H.; Vashi, R. T., Chapter 3 - Feasibility of Naturally Prepared Adsorbent. In *Characterization and Treatment of Textile Wastewater*, Patel, H.; Vashi, R. T., Eds. Elsevier: Boston, 2015; pp 73-110.

22. Bruzzoniti, M. C.; Appendini, M.; Onida, B.; Castiglioni, M.; Del Bubba, M.; Vanzetti, L.; Jana, P.; Sorarù, G. D.; Rivoira, L., Regenerable, innovative porous silicon-based polymer-derived ceramics for removal of methylene blue and rhodamine B from textile and environmental waters. *Environmental Science and Pollution Research* 2018, *25* (11), 10619-10629.

23. Richardson, M., *Chemical safety: international reference manual*. John Wiley & Sons: 2008.

24. Rafatullah, M.; Sulaiman, O.; Hashim, R.; Ahmad, A., Adsorption of methylene blue on low-cost adsorbents: a review. *Journal of hazardous materials* 2010, *177* (1-3), 70-80.

25. Bruzzoniti, M. C.; Appendini, M.; Rivoira, L.; Onida, B.; Del Bubba, M.; Jana, P.; Sorarù, G. D., Polymer-derived ceramic aerogels as sorbent materials for the removal of organic dyes from aqueous solutions. *Journal of the American Ceramic Society* 2018, *101* (2), 821-830.

26. Umoren, S.; Etim, U.; Israel, A., Adsorption of methylene blue from industrial effluent using poly (vinyl alcohol). *J. Mater. Environ. Sci* 2013, *4* (1), 75-86.

27. Tan, I.; Hameed, B.; Ahmad, A., Equilibrium and kinetic studies on basic dye adsorption by oil palm fibre activated carbon. *Chemical Engineering Journal* 2007, *127* (1-3), 111-119.

28. Zeydanli, D.; Akman, S.; Vakifahmetoglu, C., Polymer-derived ceramic adsorbent for pollutant removal from water. *Journal of the American Ceramic Society* 2018, *101* (6), 2258-2265.

29. Hojamberdiev, M.; Prasad, R. M.; Morita, K.; Schiavon, M. A.; Riedel, R., Polymer-derived mesoporous SiOC/ZnO nanocomposite for the purification of

water contaminated with organic dyes. *Microporous and Mesoporous Materials* 2012, *151*, 330-338.

30. Pan, J.; Shen, W.; Zhao, Y.; Sun, H.; Guo, T.; Cheng, Y.; Zhao, N.; Tang, H.; Yan, X., Difunctional hierarchical porous SiOC composites from silicone resin and rice husk for efficient adsorption and as a catalyst support. *Colloids and Surfaces A: Physicochemical and Engineering Aspects* 2020, *584*, 124041.

31. Ahmad, T.; Danish, M.; Rafatullah, M.; Ghazali, A.; Sulaiman, O.; Hashim, R.; Ibrahim, M. N. M., The use of date palm as a potential adsorbent for wastewater treatment: a review. *Environmental Science and Pollution Research* 2012, *19* (5), 1464-1484.

32. Guo, H.; Jiao, T.; Zhang, Q.; Guo, W.; Peng, Q.; Yan, X., Preparation of graphene oxide-based hydrogels as efficient dye adsorbents for wastewater treatment. *Nanoscale research letters* 2015, *10* (1), 272.

33. Xu, Y.; Ren, B.; Wang, R.; Zhang, L.; Jiao, T.; Liu, Z., Facile preparation of rod-like MnO nanomixtures via hydrothermal approach and highly efficient removal of methylene blue for wastewater Treatment. *Nanomaterials* 2019, *9* (1), 10.

34. Charanpahari, A.; Gupta, N.; Devthade, V.; Ghugal, S.; Bhatt, J., Ecofriendly Nanomaterials for Sustainable Photocatalytic Decontamination of Organics and Bacteria. *Handbook of Ecomaterials* 2018, 1-29.

35. Fazal, T.; Razzaq, A.; Javed, F.; Hafeez, A.; Rashid, N.; Amjad, U. S.; Rehman, M. S. U.; Faisal, A.; Rehman, F., Integrating adsorption and photocatalysis: A cost effective strategy for textile wastewater treatment using hybrid biochar-TiO2 composite. *Journal of hazardous materials* 2019, 121623.

36. Mostafapour, F. K.; Balarak, D.; Baniasadi, M., Removal of ciprofloxacin from of pharmaceutical wastewater by adsorption on SiO2 nanoparticle. *Journal of Pharmaceutical Research International* 2018, 1-9.

37. Kannan, N.; Sundaram, M. M., Kinetics and mechanism of removal of methylene blue by adsorption on various carbons—a comparative study. *Dyes and pigments* 2001, *51* (1), 25-40.

38. Ali, I.; Gupta, V., Advances in water treatment by adsorption technology. *Nature protocols* 2006, *1* (6), 2661.

39. Gupta, V. K.; Kumar, R.; Nayak, A.; Saleh, T. A.; Barakat, M., Adsorptive removal of dyes from aqueous solution onto carbon nanotubes: a review. *Advances in colloid and interface science* 2013, *193*, 24-34.

40. Jenne, E. A., *Adsorption of metals by geomedia: data analysis, modeling, controlling factors, and related issues*. Academic Press: San Diego: 1998.

41. Lavrenko, V.; Podchernyaeva, I.; Shchur, D.; Zolotarenko, A. D.; Zolotarenko, A. D., Features of Physical and Chemical Adsorption During Interaction of Polycrystalline and Nanocrystalline Materials with Gases. *Powder Metallurgy and Metal Ceramics* 2018, *56* (9-10), 504-511.

42. Banerjee, S.; Gautam, R. K.; Jaiswal, A.; Chattopadhyaya, M. C.; Sharma, Y. C., Rapid scavenging of methylene blue dye from a liquid phase by adsorption on alumina nanoparticles. *RSC Advances* 2015, *5* (19), 14425-14440.

43. Gaikwad, R.; Misal, S., Sorption studies of methylene blue on silica gel. *International Journal of Chemical Engineering and Applications* 2010, *1* (4), 342.

44. Han, R.; Zhang, J.; Han, P.; Wang, Y.; Zhao, Z.; Tang, M., Study of equilibrium, kinetic and thermodynamic parameters about methylene blue adsorption onto natural zeolite. *Chemical Engineering Journal* 2009, *145* (3), 496-504.

45. Vakifahmetoglu, C., Zeolite decorated highly porous acicular calcium silicate ceramics. *Ceramics International* 2014, *40* (8), 11925-11932.

46. Ahmad, A.; Loh, M.; Aziz, J., Preparation and characterization of activated carbon from oil palm wood and its evaluation on methylene blue adsorption. *Dyes and pigments* 2007, *75* (2), 263-272.

47. Yang, S.-T.; Chen, S.; Chang, Y.; Cao, A.; Liu, Y.; Wang, H., Removal of methylene blue from aqueous solution by graphene oxide. *Journal of colloid and interface science* 2011, *359* (1), 24-29.

48. Bhatkhande, D. S.; Pangarkar, V. G.; Beenackers, A. A. C. M., Photocatalytic degradation for environmental applications–a review. *Journal of Chemical*

Technology & Biotechnology: International Research in Process, Environmental & Clean Technology 2002, *77* (1), 102-116.

49. Umar, M.; Aziz, H. A., Photocatalytic degradation of organic pollutants in water. *Organic pollutants-monitoring, risk and treatment* 2013, *8*, 196-197.

50. Wang, R.; Shi, K.; Huang, D.; Zhang, J.; An, S., Synthesis and degradation kinetics of TiO 2/GO composites with highly efficient activity for adsorption and photocatalytic degradation of MB. *Scientific Reports* 2019, *9* (1), 1-9.

51. Sakthivel, S.; Neppolian, B.; Shankar, M.; Arabindoo, B.; Palanichamy, M.; Murugesan, V., Solar photocatalytic degradation of azo dye: comparison of photocatalytic efficiency of ZnO and TiO2. *Solar energy materials and solar cells* 2003, *77* (1), 65-82.

52. Vakifahmetoglu, C.; Semerci, T.; Soraru, G. D., Closed porosity ceramics and glasses. *Journal of the American Ceramic Society* 2020.

53. Nalbantoğlu, A. İlaç taşıyıcı sistem olarak katı lipit nanopartiküllerin hazırlanması ve in-vitro değerlendirilmesi. Marmara University, 2016.

54. Batıgöç, Ç. Yüzey aktif maddelerinin etkileşimlerinin ve fiziksel özelliklerinin incelenmesi. Trakya University, 2010

55. Asua, J. M., Miniemulsion Polymerization. In *Encyclopedia of Polymeric Nanomaterials*, Kobayashi, S.; Müllen, K., Eds. Springer Berlin Heidelberg: Berlin, Heidelberg, 2015; pp 1267-1275.

56. Slomkowski, S.; Alemán, J. V.; Gilbert, R. G.; Hess, M.; Horie, K.; Jones, R. G.; Kubisa, P.; Meisel, I.; Mormann, W.; Penczek, S., Terminology of polymers and polymerization processes in dispersed systems (IUPAC Recommendations 2011). *Pure and Applied Chemistry* 2011, *83* (12), 2229-2259.

57. Gupta, A.; Eral, H. B.; Hatton, T. A.; Doyle, P. S., Nanoemulsions: formation, properties and applications. *Soft matter* 2016, *12* (11), 2826-2841.

58. Singh, Y.; Meher, J. G.; Raval, K.; Khan, F. A.; Chaurasia, M.; Jain, N. K.; Chourasia, M. K., Nanoemulsion: Concepts, development and applications in drug delivery. *Journal of controlled release* 2017, *252*, 28-49.

59. Zhang, J., Novel emulsion-based delivery systems. 2011.

60. Santhosh, B.; Vakifahmetoglu, C.; Ionescu, E.; Reitz, A.; Albert, B.; Soraru, G. D., Processing and thermal characterization of polymer derived SiCN (O) and SiOC reticulated foams. *Ceramics International* 2020, *46* (5), 5594-5601.

61. Ionescu, E.; Kleebe, H.-J.; Riedel, R., Silicon-containing polymer-derived ceramic nanocomposites (PDC-NCs): Preparative approaches and properties. *Chemical Society Reviews* 2012, *41* (15), 5032-5052.

62. Assefa, D.; Zera, E.; Campostrini, R.; Soraru, G. D.; Vakifahmetoglu, C., Polymer-derived SiOC aerogel with hierarchical porosity through HF etching. *Ceramics International* 2016, *42* (10), 11805-11809.

63. Vakifahmetoglu, C. Fabrication and characterization of porous ceramics with hierarchical porosity. University of Padua, 2010.

64. Colombo, P., *Polymer derived ceramics: from nano-structure to applications*. DEStech Publications, Inc: 2010.

65. Adam, M.; Vakifahmetoglu, C.; Colombo, P.; Wilhelm, M.; Grathwohl, G., Polysiloxane-derived ceramics containing nanowires with catalytically active tips. *Journal of the American Ceramic Society* 2014, *97* (3), 959-966.

66. Vakifahmetoglu, C.; Balliana, M.; Colombo, P., Ceramic foams and micro-beads from emulsions of a preceramic polymer. *Journal of the European Ceramic Society* 2011, *31* (8), 1481-1490.

67. Vakifahmetoglu, C.; Zeydanli, D.; Colombo, P., Porous polymer derived ceramics. *Materials Science and Engineering: R: Reports* 2016, *106*, 1-30.

68. Barroso, G.; Li, Q.; Bordia, R. K.; Motz, G., Polymeric and ceramic silicon-based coatings–a review. *Journal of materials chemistry A* 2019, *7* (5), 1936-1963.

69. Kumar, B. M.; Kim, Y.-W., Processing of polysiloxane-derived porous ceramics: a review. *Science and technology of advanced materials* 2010, *11* (4), 044303.

70. Colombo, P.; Mera, G.; Riedel, R.; Soraru, G. D., Polymer-derived ceramics: 40 years of research and innovation in advanced ceramics. *Journal of the American Ceramic Society* 2010, *93* (7), 1805-1837.

71. Vakifahmetoglu, C.; Zeydanli, D.; Ozalp, V. C.; Borsa, B. A.; Soraru, G. D., Hierarchically porous polymer derived ceramics: A promising platform for multidrug delivery systems. *Materials & Design* 2018, *140*, 37-44.

72. Wen, Q.; Yu, Z.; Riedel, R., The Fate and Role of in situ Formed Carbon in Polymer-Derived Ceramics. *Progress in Materials Science* 2019, 100623.

73. Lu, K.; Erb, D., Polymer derived silicon oxycarbide-based coatings. *International Materials Reviews* 2018, *63* (3), 139-161.

74. Stabler, C. Mechanical and Thermal Properties of SiOC-based Glasses and Glass Ceramics. Technische Universität, 2019.

75. Stabler, C.; Ionescu, E.; Graczyk-Zajac, M.; Gonzalo-Juan, I.; Riedel, R., Silicon oxycarbide glasses and glass-ceramics:"All-Rounder" materials for advanced structural and functional applications. *Journal of the American Ceramic Society* 2018, *101* (11), 4817-4856.

76. Godoy, N. V.; Segatelli, M. G., Kinetic investigation of thermal formation processes of SiOC glasses derived from C-containing hybrid polymeric networks. *Journal of the Brazilian Chemical Society* 2015, *26* (5), 899-909.

77. Fortuniak, W.; Pospiech, P.; Mizerska, U.; Chojnowski, J.; Slomkowski, S.; Nyczyk-Malinowska, A.; Lach, R.; Hasik, M., SiCO ceramic microspheres produced by emulsion processing and pyrolysis of polysiloxanes of various structures. *Ceramics International* 2016, *42* (10), 11654-11665.

78. Fortuniak, W.; Chojnowski, J.; Slomkowski, S.; Nyczyk-Malinowska, A.; Pospiech, P.; Mizerska, U., Solid ceramic SiCO microspheres and porous rigid siloxane microspheres from swellable polysiloxane particles. *Materials Chemistry and Physics* 2015, *155*, 83-91.

79. Wasan Awin, E.; Lale, A.; Kumar, K. C. N. H.; Bilge Demirci, U.; Bernard, S.; Kumar, R., Novel precursor-derived meso-/macroporous TiO2/SiOC nanocomposites with highly stable anatase nanophase providing visible light photocatalytic activity and superior adsorption of organic dyes. *Materials* 2018, *11* (3), 362.

80. Dire, S.; Tagliazucca, V.; Salvadori, L.; Soraru, G. D., Preparation of Dense and Porous Silicon Oxycarbide Submicrometer-Sized Spheres Using a Modified Stöber Process. *Journal of the American Ceramic Society* 2011, *94* (11), 3819-3824.

81. Fukui, H.; Ohsuka, H.; Hino, T.; Kanamura, K., A Si− O− C composite anode: high capability and proposed mechanism of lithium storage associated with microstructural characteristics. *ACS applied materials & interfaces* 2010, *2* (4), 998-1008.

82. Lu, K.; Erb, D.; Liu, M., Phase transformation, oxidation stability, and electrical conductivity of TiO 2-polysiloxane derived ceramics. *Journal of Materials Science* 2016, *51* (22), 10166-10177.

83. Ye, C.; Chen, A.; Colombo, P.; Martinez, C., Ceramic microparticles and capsules via microfluidic processing of a preceramic polymer. *Journal of The Royal Society Interface* 2010, *7* (suppl_4), S461-S473.

84. Ahmad, Z.; Nangrejo, M.; Edirisinghe, M.; Stride, E.; Colombo, P.; Zhang, H., Engineering a material for biomedical applications with electric field assisted processing. *Applied Physics A* 2009, *97* (1), 31-37.

85. Tolosa, A.; Krüner, B.; Jäckel, N.; Aslan, M.; Vakifahmetoglu, C.; Presser, V., Electrospinning and electrospraying of silicon oxycarbide-derived nanoporous carbon for supercapacitor electrodes. *Journal of Power Sources* 2016, *313*, 178-188.

86. Weinberger, M.; Pfeifer, C.; Schindler, S.; Diemant, T.; Behm, R. J.; Wohlfahrt-Mehrens, M., Submicron-sized silicon oxycarbide spheres as anodes for alkali ion batteries. *Journal of Materials Chemistry A* 2015, *3* (47), 23707-23715.

87. Sang, Z.; Su, D.; Wang, J.; Liu, Y.; Ji, H., Bi-continuous nanoporous carbon sphere derived from SiOC as high-performance anodes for PIBs. *Chemical Engineering Journal* 2020, *381*, 122677.

88. Liu, C.; Meng, X.; Zhang, X.; Hong, C.; Han, J.; Han, W.; Xu, B.; Dong, S.; Du, S., High temperature structure evolution of macroporous SiOC ceramics prepared by a sol–gel method. *Ceramics International* 2015, *41* (9), 11091-11096.

89. Szymanski, W.; Lipa, S.; Fortuniak, W.; Chojnowski, J.; Pospiech, P.; Mizerska, U.; Slomkowski, S.; Nyczyk-Malinowska, A.; Hasik, M., Silicon oxycarbide (SiOC) ceramic microspheres–Structure and mechanical properties by nanoindentation studies. *Ceramics International* 2019, *45* (9), 11946-11954.

90. Yu, Y.; Wang, H.; San, H.; Liu, Y.; Fang, J.; An, L.; Fang, Q., A Facile Route to Construct S i CO Nanospheres with Tunable Sizes. *International Journal of Applied Ceramic Technology* 2014, *11* (4), 670-675.

91. Bakumov, V.; Schwarz, M.; Kroke, E., Emulsion processing of polymer-derived porous Si/C/(O) ceramic bodies. *Journal of the European Ceramic Society* 2009, *29* (13), 2857-2865.

92. Fortuniak, W.; Pospiech, P.; Mizerska, U.; Chojnowski, J.; Slomkowski, S.; Nyczyk-Malinowska, A.; Wojteczko, A.; Wisla-Walsh, E.; Hasik, M., Generation of meso-and microporous structures by pyrolysis of polysiloxane microspheres and by HF etching of SiOC microspheres. *Ceramics International* 2018, *44* (1), 374-383.

93. Bakumov, V.; Schwarz, M.; Kroke, E., Emulsion Processing and Size Control of Polymer-derived Spherical Si/C/O Ceramic Particles. *Soft Materials* 2007, *4* (2-4), 287-299.

94. Chojnowski, J.; Slomkowski, S.; Fortuniak, W.; Mizerska, U.; Pospiech, P., Hydrophilic Polysiloxane Microspheres and Ceramic SiOC Microspheres Derived from Them. *Journal of Inorganic and Organometallic Polymers and Materials* 2020, *30* (1), 56-68.

95. Weinberger, M.; Munding, J.; Lindén, M.; Wohlfahrt-Mehrens, M., Template-Derived Submicrometric Carbon Spheres for Lithium–Sulfur and Sodium-Ion Battery Electrodes. *Energy Technology* 2018, *6* (9), 1797-1804.

96. Hourlier, D.; Venkatachalam, S.; Ammar, M.-R.; Blum, Y., Pyrolytic conversion of organopolysiloxanes. *Journal of Analytical and Applied Pyrolysis* 2017, *123*, 296-306.

97. Vakifahmetoglu, C.; Zeydanli, D.; de Mello Innocentini, M. D.; dos Santos Ribeiro, F.; Lasso, P. R. O.; Soraru, G. D., Gradient-hierarchic-aligned porosity SiOC ceramics. *Scientific reports* 2017, *7* (1), 1-12.

98. Nedunchezhian, S.; Sujith, R.; Kumar, R., Processing and characterization of polymer precursor derived silicon oxycarbide ceramic foams and compacts. *Journal of Advanced Ceramics* 2013, *2* (4), 318-324.

99. Gelest. https://www.gelest.com/ (Accessed 19.05.2020).

100. Mera, G.; Gallei, M.; Bernard, S.; Ionescu, E., Ceramic nanocomposites from tailor-made preceramic polymers. *Nanomaterials* 2015, *5* (2), 468-540.

101. Hojamberdiev, M.; Prasad, R. M.; Morita, K.; Zhu, Y.; Schiavon, M. A.; Gurlo, A.; Riedel, R., Template-free synthesis of polymer-derived mesoporous SiOC/TiO2 and SiOC/N-doped TiO2 ceramic composites for application in the removal of organic dyes from contaminated water. *Applied Catalysis B: Environmental* 2012, *115*, 303-313.

102. Kumar, K. V.; Porkodi, K.; Rocha, F., Langmuir–Hinshelwood kinetics–a theoretical study. *Catalysis Communications* 2008, *9* (1), 82-84.

103. Fredrick, E.; Walstra, P.; Dewettinck, K., Factors governing partial coalescence in oil-in-water emulsions. *Advances in Colloid and Interface Science* 2010, *153* (1-2), 30-42.

104. ASTM, D., 3576, Standard test method for cell size of rigid cellular plastics. *Annual book of ASTM standards 8*.

105. Wang, L.; Lu, K.; Ma, R., Effects of different polymer precursors on the characteristics of SiOC bulk ceramics. *Applied Physics A* 2019, *125* (6), 395.

106. Su, D.; Li, Y.-L.; An, H.-J.; Liu, X.; Hou, F.; Li, J.-Y.; Fu, X., Pyrolytic transformation of liquid precursors to shaped bulk ceramics. *Journal of the European Ceramic Society* 2010, *30* (6), 1503-1511.

107. Satoru, I.; Toshiyuki, N.; Hidehiko, T., Precipitation processing to synthesize fine polycarbosilane particles for precursors of silicon carbide powders. *Journal of the Ceramic Society of Japan* 2006, *114* (1330), 507-510.

108. Vakifahmetoglu, C.; Buldu, M.; Karakuscu, A.; Ponzoni, A.; Assefa, D.; Soraru, G. D., High surface area carbonous components from emulsion derived SiOC and their gas sensing behavior. *Journal of the European Ceramic Society* 2015, *35* (16), 4447-4452.

109. Bhaskar, S.; Awin, E. W.; Kumar, K. H.; Lale, A.; Bernard, S.; Kumar, R., Design of nanoscaled heterojunctions in precursor-derived t-ZrO 2/SiOC (N) nanocomposites: Transgressing the boundaries of catalytic activity from UV to visible light. *Scientific Reports* 2020, *10* (1), 1-13.

110. Dubey, R. J. C.; Sasikumar, P. V. W.; Krumeich, F.; Blugan, G.; Kuebler, J.; Kravchyk, K. V.; Graule, T.; Kovalenko, M. V., Silicon Oxycarbide—Tin Nanocomposite as a High-Power-Density Anode for Li-Ion Batteries. *Advanced Science* 2019, *6* (19), 1901220.

111. Mirabedini, A.; Mirabedini, S.; Babalou, A.; Pazokifard, S., Synthesis, characterization and enhanced photocatalytic activity of TiO_2/SiO_2 nanocomposite in an aqueous solution and acrylic-based coatings. *Prog. Org. Coat.* 2011, *72* (3), 453-460.

112. Rasalingam, S.; Peng, R.; Koodali, R. T., Removal of hazardous pollutants from wastewaters: applications of TiO2-SiO2 mixed oxide materials. *Journal of Nanomaterials* 2014, *2014*.

113. Scuderi, V.; Buccheri, M.; Impellizzeri, G.; Di Mauro, A.; Rappazzo, G.; Bergum, K.; Svensson, B. G.; Privitera, V., Photocatalytic and antibacterial properties of titanium dioxide flat film. *Materials Science in Semiconductor Processing* 2016, *42*, 32-35.